# Numerical-relativity simulations of the quasi-circular inspiral and merger of non-spinning, charged black holes: methods and comparison with approximate approaches

Gabriele Bozzola[1,*] and Vasileios Paschalidis[1,2,†]

[1] *Department of Astronomy, University of Arizona, Tucson, AZ, USA*
[2] *Department of Physics, University of Arizona, Tucson, AZ, USA*

(Dated: June 7, 2021)

We present fully general relativistic simulations of the quasi-circular inspiral and merger of charged, non-spinning, binary black holes with charge-to-mass ratio $\lambda \leq 0.3$. We discuss the key features that enabled long term and stable evolutions of these binaries. We also present a formalism for computing the angular momentum carried away by electromagnetic waves, and the electromagnetic contribution to black-hole horizon properties. We implement our formalism and present the results for the first time in numerical-relativity simulations. In addition, we compare our full non-linear solutions with existing approximate models for the inspiral and ringdown phases. We show that Newtonian models based on the quadrupole approximation have errors of 20 %–100 % in key gauge-invariant quantities. On the other hand, for the systems considered, we find that estimates of the remnant black hole spin based on the motion of test particles in Kerr-Newman spacetimes agree with our non-linear calculations to within a few percent. Finally, we discuss the prospects for detecting black hole charge by future gravitational-wave detectors using either the inspiral-merger-ringdown signal or the ringdown signal alone.

## I. INTRODUCTION

In previous work [1, 2], we initiated a systematic program to study the interactions between charged black holes in full non-linear Einstein-Maxwell theory. These explorations are relevant for gravitational-wave astronomy, exotic astrophysics, and fundamental physics (such as modified gravity and beyond-standard-model physics). We first review these applications in Sec. I A. We summarize the main goals and results of this work in Sec. I B, and outline the structure of the manuscript and conventions adopted in Sec. I C. Readers that are mainly interested in our new results can skip Sec. I A.

### A. Motivation for non-linear simulations in Einstein-Maxwell theory

Over the past few years there has been a growing interest in modified theories of gravity to perform strong-field tests of general relativity. The data collected by the Event Horizon Telescope [3] allowed for new tests of gravity around supermassive black holes, and the observation of gravitational waves by the LIGO-Virgo collaboration [4] enabled the first constraints on deviations from Einstein's theory in the highly dynamical strong-field regime (see, e.g. [5–8]). In turn, this latter achievement was made possible by advancements in the field of numerical relativity that has been able to produce the accurate gravitational-wave models that are needed to detect these signals and perform the associated parameter estimations. Therefore, it should come to no surprise that the scarcity of simulations of compact binary mergers in modified theories of gravity [9] severely limits out our ability to use gravitational-wave observations to place stronger constraints. The reason for this shortage is that many models of modified gravity are "sick" (e.g., lack of well-posedness, ghosts, etc., see [10] for a discussion), thereby making these computations particularly challenging or impossible. Hence, with the exception of a few cases [11–13], progress in this direction is usually made by means of order-reduced approaches, and not solutions of the full theory (see, e.g. [14–18]). In contrast to modified gravity, Einstein-Maxwell theory admits a well-posed initial-value problem, while sharing other non-trivial properties with modified gravity (e.g, emission of dipole radiation[1]). Moreover, some modified gravity theories reduce effectively to Einstein-Maxwell in specific limits (e.g. [19]). Therefore, the inspiral and merger of charged black holes constitutes, in a sense, the middle ground between traditional general relativity and modified theories of gravity. Despite these facts, the non-linear dynamics of charged binary black holes is uncharted territory, with [20–24] being the main works on the subject.

Studying charged black holes in Einstein-Maxwell theory not only provides a way to capture some features of specific modified theories in a controlled environment, but also simulations of such systems have direct astrophysical and fundamental physics applications. First, while black holes are expected to be electrically neutral [25–29], there is no definitive observational sup-

* gabrielebozzola@arizona.edu
† vpaschal@arizona.edu

[1] We note that this is not gravitational dipole radiation.

port for this expectation. Therefore, this assumption must be tested. Gravitational-wave observations offer a model-independent way to test this assumption. Second, "charge" is an umbrella term that applies to different models in exotic astrophysics and beyond-standard-model physics, including dark matter with hidden charge and interacting with dark electromagnetism (e.g. [30–36] or dark matter with fractional charge [37–46]), as well as modified theories of gravity with additional vector fields sourced by a "gravitational" charge [19]. Furthermore, through a duality transformation, "charge" can also be interpreted as *magnetic charge*. Recently, black holes with magnetic charge in astrophysics have received some attention (e.g. [47–51]), with focus on primordial black holes in [47, 48]. Gravitational waves can be used to directly test whether black holes have any kind of charge. This was the goal of our previous paper on the subject [2], where we found that charge-to-mass ratios of up to $\lambda = 0.3$[2] are compatible with GW150914 [52], assuming that the role of black hole spins can be neglected. Upper bounds on black hole charge can be translated to constraints on the properties of the dark matter particles in the aforementioned models or on the parameters of modified gravity theories [2].

Numerical-relativity simulations of charged black holes can be used to produce gravitational-wave templates that include charge (for example, by *hybridizing* analytical waveforms with numerical ones, as done in [53–58]). Since the detection of gravitational waves by the LIGO-Virgo interferometers relies heavily on matched-filtering techniques [59–61], extended gravitational-wave template banks that encode additional physics are necessary for the parameter estimation [55, 62–65]. A phenomenological model based on numerical relativity with charge can also be used in Bayesian analyses to directly constrain this parameter in LIGO-Virgo signals.

Finally, charge provides a way for a black hole to reach extremality (along with the spin). Thus, non-linear studies of charged binary black holes offer new pathways to investigate cosmic censorship in conditions where it has never been probed before. For instance, it would be of interest to tackle the question: "can black holes be overcharged?", going beyond previous perturbative approaches [66, 67].

### B. Goals of this work

In this paper, we continue our explorations of the non-linear interaction of charged black holes by approaching the problem of inspirals and mergers on two different thrusts. On one side, we present necessary ingredients for performing long-term and stable numerical relativity simulations of the quasi-circular inspiral of charged binary black holes. In particular, we discuss how Kreiss-Oliger dissipation [68] helps (or impedes) these evolutions. We also describe the formalism that we adopt for our evolutions detailing some features that have not been included in previous works (e.g., the computation of the angular momentum carried away by electromagnetic waves with the Newman-Penrose formalism, and the contribution of electromagnetic fields to the quasi-local spin of a black hole). Using the gravitational waveforms generated by our simulations, we explore black hole charge detectability by future ground- and space-based gravitational wave detectors. The second thrust of this work consists of analyzing existing approximate models for the inspiral of charged black hole binaries and their remnant black holes, and comparing them with our non-linear solutions.

In [2], we presented the first simulations of the quasi-circular inspiral and merger of charged black holes in full general relativity with valid initial data. Here, we present more details about these computations. We focus on systems with mass ratio $q = 29/36$, as inferred for GW150914 [52, 69], and restrict the charge-to-mass ratio $\lambda$ of the individual black holes to values $|\lambda| \leq 0.3$. The mass ratio is close to unity, so we expect that the conclusions presented in this work will hold for equal-mass binaries. We consider three systems: (1) binary black holes with same charge-to-mass ratio in magnitude and sign, (2) binary black holes with charge-to-mass ratio equal in magnitude but oppositely charged, and (3) binary black holes in which only the primary is charged. In this first exploration, we do not study cases where the black holes have different (non-zero) charge-to-mass ratio $\lambda$.

For the comparison of our solutions with existing approximations for the inspiral phase, we consider a model that is based on Newtonian physics coupled with the quadrupole formula to incorporate radiation reaction. We will refer to this model with the letters "QA" (*quadrupole approximation*). Given its simplicity, this model has been routinely used to study the merger of charged black holes (e.g. [36, 44, 47–49, 70, 71]). Prior work on head-on collisions of charged black hole reported good agreement in some quantities between these approximate calculations and full non-linear simulations [20, 21]. Therefore, a goal of this work is to determine the errors of the Newtonian approximation when applied to the quasi-circular inspiral of charged black holes. A key result of our study is that Newtonian models can be successfully applied to obtain order-of-magnitude estimates of observables or to build intuition, but they cannot be used for precision studies of these mergers.

A second focus of this paper is on the properties of the post-merger black hole and its quasi-normal modes. This is especially relevant for LISA, which will detect the ringdown signal arising from the merger of supermassive black holes with high signal-to-noise ratio [72]. The quasi-normal modes can be used to test general relativity [73], as their characteristic frequencies depend on

[2] We are using geometrized units. See Sec. I C

the spin, mass, and charge of the remnant black hole in a known way. Here, we consider the method described in [74] to estimate the remnant black hole spin using conservation arguments, and we compare it with our non-linear solutions. As we discuss later, we find that the quasi-normal-mode properties do not change much across the simulations considered here. This is due to the value of the final spin and to the relatively weak dependence of the quasi-normal-modes on the charge for the values of $\lambda$ we consider.

### C. Structure of the paper and conventions

The structure of the remainder of the paper is the following. In Sec. II, we describe the formalism that we adopt to perform simulations of the quasi-circular inspiral and merger of charged black holes. In particular, we discuss how to obtain stable quasi-circular inspirals, and highlight some new features of the approach. Next (Sec. III), we outline the simplest (Newtonian) model for the quasi-circular inspiral of non-spinning, charged binary black holes. Sec. IV describes what we can say about the remnant black hole using results of relativistic calculations and perturbation theory. In Sec. V, we follow the black holes through their coalescence: first (Sec. V A) we study the inspiral and compare the non-linear solution with the Newtonian model, then (Sec. V B) we discuss results from the full simulations, and finally (Sec. V C) we report on the properties of the remnant black hole. Conclusions and future directions are collected in Sec. VI.

We adopt geometrized units with $G = c = 1$, with $G$ being Newton's constant and $c$ the speed of light in vacuum. We also adopt Gaussian units for the electromagnetic sector. Similarly, we denote the different simulations adding a superscript and a subscript when we report physical quantities. For example, $e^+_+$, $e^+_-$, and $e^+_0$ indicate the eccentricity measured in the evolutions where black holes have charges with the same signs, with opposite signs, and only one charged black hole, respectively.[3] In geometrized units, quantities have units of length. Here we report all the results in units of the Arnowitt-Deser-Misner (ADM) mass of the system $M$ [75]. We use the letters $a, b, c, d$ for spacetime indices, and $i, j, k$ for spatial ones. For everything else, we follow the same conventions as in [76].

[3] For figures reporting different charge-to-mass ratios, we use a consistent style: red dashed lines with circles are for systems with both black holes charged with the same sign, blue dotted lines with squares are for oppositely charged ones, and green dash dotted lines with triangles are for evolutions in which only one black hole is charged.

## II. METHODS AND FORMALISM

In this section, we describe the methods we adopt for solving the full non-linear Einstein-Maxwell equations (Sec. II A). We discuss our approach to building quasi-circular initial data (Sec. II B) and how to achieve long-term, stable evolutions (Sec. II C). We also describe the formalism and implementation of two new features that have not appeared in previous simulations: the contribution of the electromagnetic fields to black-hole horizon properties (Sec. II D), and the angular momentum carried away by electromagnetic waves (Sec. II E).

### A. Equations and numerical setup

In this paper, we study systems described by the source-free Einstein-Maxwell equations [77] (electrovacuum[4])

$$\mathcal{R}_{ab} - \frac{1}{2} g_{ab} \mathcal{R} = 8\pi T^{\rm EM}_{ab} \,, \tag{1a}$$

$$\nabla_a F^{ab} = 0 \,, \tag{1b}$$

$$\nabla_a {}^\star F^{ab} = 0 \,, \tag{1c}$$

where $\mathcal{R}_{ab}$ is the Ricci tensor associated with the metric $g_{ab}$, $\mathcal{R} = \mathcal{R}^a_{\ a}$, $F_{ab} = 2\, A_{[a,b]}$ is the Maxwell field-strength tensor, with $A_a$ the electromagnetic four-vector potential, and ${}^\star F_{ab}$ is its Hodge dual, defined by

$${}^\star F^{ab} = \frac{1}{2} \epsilon^{abcd} F_{cd} \,, \tag{2}$$

with $\epsilon^{abcd}$ being the Levi-Civita tensor. The electromagnetic stress-energy tensor is given by

$$4\pi T^{\rm EM}_{ab} = F_{ac} F_{bd} g^{cd} - \frac{1}{4} g_{ab} F_{cd} F^{cd} \,. \tag{3}$$

We solve the coupled Einstein-Maxwell equations in a 3+1 decomposition of the spacetime (for more details, see Sec. II A in [1], or textbooks on the subject, e.g. [79–81]) and use the `Einstein Toolkit` [82–84] for the numerical integration.

The initial data are generated by `TwoChargedPunctures`, which solves the Hamiltonian constraint equation using a Bowen-York approach [85, 86]. We developed and tested `TwoChargedPunctures` in [1], starting from the widely used `TwoPunctures` code [87]. `TwoChargedPunctures` takes as input the locations, charges, bare masses, angular, and linear momenta of each of the two black

[4] In all our discussion, we assume that the black holes are in vacuum (see [78] for a discussion on the role of the environment). We also ignore Schwinger pair-production and any other quantum effects.

holes, and it can build arbitrary configurations. We start our simulations at a coordinate distance of $12.1\,M$, with the two black holes having fixed charge-to-mass ratio $\lambda$ and mass-ratio 29/36. In this first study, we only explore systems with the two black holes having the same $\lambda$ (up to the sign), or with only one charged black hole. In Sec. II B, we discuss how to choose the initial data parameters to achieve quasi-circular inspirals.

The evolution of the spacetime is performed with the `Lean` code [88], which implements the Baumgarte-Shapiro-Shibata-Nakamura (BSSN) formulation of Einstein's equations [89, 90]. `Lean` evolves the conformal factor $\chi_{\rm conf} = \gamma^{-1/6}$, with $\gamma$ determinant of the 3-metric. We adopt as spacetime gauges the $1+\log$ and the $\Gamma-$ driver conditions [91, 92]. The electromagnetic fields are evolved with the massless version of the `ProcaEvolve` [23] code. The code evolves the electric field $E^i$, the scalar and vector potentials $\phi$ and $A_i$, along with an auxiliary variable $Z$ that is used to control the Maxwell constraints. The precise equations solved by `ProcaEvolve` are presented in the Appendix of [23]. These codes are publicly available as part of the Canuda suite [93, 94] and have been extensively tested and used throughout the years. We use sixth-order accurate finite differences for the spatial derivative, and we integrate in time with a fourth-order Runge-Kutta method.

Apparent horizons are located using `AHFinderDirect` [95, 96], and their physical properties are measured with `QuasiLocalMeasuresEM`, a version of `QuasiLocalMeasures` [97] updated to implement the isolated horizon formalism in full Einstein-Maxwell theory (see Sec. II C in [1]). This extension is necessary when considering black holes in the presence of electromagnetic fields, as we discuss in Sec. II D.

We extract waves via the Newman-Penrose formalism as implemented in `NPScalars_Proca` (see, Sec. II E) and recover the gravitational-wave strain with a time integration using the fixed frequency integration method [98]. We consider a finite extraction radius of $110.69\,M$. Results are approximately invariant if we consider different extraction radii or if we extrapolate the waves to infinity with the method described in [65].

We work with Cartesian grids with Berger-Oliger adaptive mesh refinement as provided by `Carpet` [99]. We use two sets of nine nested refinement levels that are centered on and track the centroid of the black hole apparent horizons. The resolution of our simulations is $M/65$, where $M$ is the total ADM mass, with additional resolutions to perform convergence study (which we reported in [2]). The outer boundary is at $1033\,M$ and we performed selected simulations to verify that the location does not affect the evolution. Some more details on evolution and grid parameters used in our simulations are reported in Appendix B.

### B. Controlling the eccentricity

In this work, we focus on quasi-circular inspirals. When considering charged black holes, the effect of the electromagnetic fields must be taken into account to achieve a low-eccentricity coalescence. Here, we describe a simple method to incorporate the effect of charge. This approach successfully yields quasi-circular inspirals for the values of $\lambda$ explored in this study.

First, it is useful to summarize how quasi-circular inspirals are obtained in the case without charge. The simplest way is to start from Newtonian physics. Consider two point particles with mass $m_1$, $m_2$, and assume that they are in a circular Keplerian orbit. The orbital angular velocity $\Omega$ of each particle is (restoring the gravitational constant $G$)

$$\Omega = \sqrt{\frac{G(m_1+m_2)}{d^3}}\,, \tag{4}$$

where $m_i$ is the mass of the $i$-th component, and $d$ the orbital separation. If we denote the mass-ratio $q = m_1/m_2$, the linear velocity of two particles becomes

$$v_1 = \frac{\Omega d}{1+q} \quad \text{and} \quad v_2 = q\frac{\Omega d}{1+q}\,. \tag{5}$$

In numerical integrations, black holes are assumed to behave like these point masses, so $p_i = m_i v_i$ is the initial linear momentum assigned to the $i$-th black hole. Evolutions initialized with such Newtonian values have significant residual eccentricity [100], hence high-order post-Newtonian (PN) expansions are used to compute more accurately the linear momenta necessary for quasi-circularity. When going beyond the Newtonian approximation, radial contribution to the velocities appear.

Now, let us endow the point particles with charges $q_1 = \lambda_1 m_1$, and $q_2 = \lambda_2 m_2$ (with $\lambda$ being the charge-to-mass ratio). In Newtonian physics, both electromagnetism and gravity are central forces, so, from the point of view of the dynamics, this system is indistinguishable from one with uncharged bodies but gravitational constant $\widetilde{G} = (1-\lambda_1\lambda_2)G$. For this reason, one can incorporate the effect of charge by rescaling $G$ to $\widetilde{G}$. We can use this fact to achieve low-eccentricity inspirals for charged black holes. First, we compute the linear momenta needed for a quasi-circular coalescence of the black holes without charges using the highest order post-Newtonian expansion available (in our simulations we used 2.5PN). Then, we rescale these momenta by $\sqrt{1-\lambda_1\lambda_2}$ to introduce the effect of electromagnetism. This simple method is effective at keeping eccentricity under control for the values of charge-to-mass ratio explored here, as we show next.

Following [100], we estimate the residual eccentricity by fitting the time derivative of the coordinate separation of the two black holes $\dot{d}$ with a function of the form

$$\dot{d}(t) = A_0 + A_1 t + B\sin(\omega t + \varphi)\,. \tag{6}$$

In Fig. 1, we show the coordinate separation $d$ and its derivative $\dot{d}$ for the most extreme simulations that we are considering here. The scale of the amplitude of the oscillations in the bottom panel already provides an idea of the (small) amount of residual eccentricity. The very beginning of the time series is noisy due to the relaxation of the initial data, so we exclude that part of the simulation. We perform the fit with the Levenberg-Marquardt algorithm [101, 102] for non-linear least-square fitting as implemented in MINPACK. As in [100], we find that fits are not perfect, so the eccentricities reported should be considered as estimates. In general, we find that the first orbit is the one with the most eccentricity. Fitting the first three orbits we find $e^+_+ \approx 0.01$, $e^+_- \approx 0.02$, and $e^+_0 \approx 0.01$. The eccentricity is significantly reduced if we consider the next three orbits after the first: $e^+_+ \approx 2\times10^{-3}$, $e^+_- \approx 4\times10^{-3}$, and $e^+_0 \approx 1\times10^{-3}$.

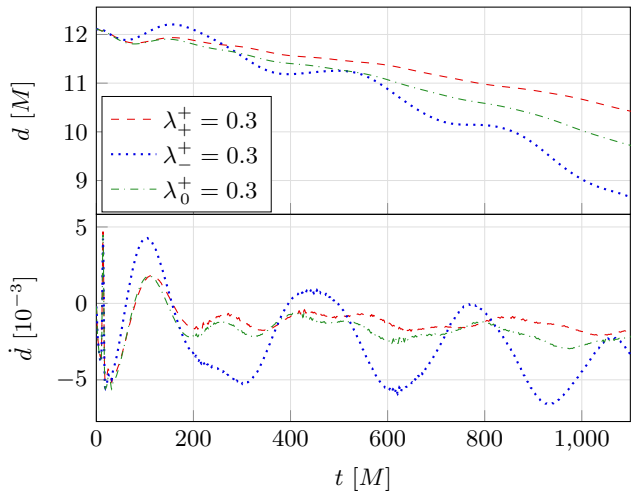


FIG. 1. First few orbits for the simulations with charge-to-mass ratio of $\lambda = 0.3$. Top panel: (coordinate) separation $d$ of the centroid of the two black holes as a function of the (coordinate) time. Bottom panel: time derivative of $d$, this quantity can be used to estimate the residual eccentricity with Eq. (6). The initial spike is due to the initial data relaxation, and is not included in our analyses. Note that these quantities are not gauge-invariant.

These values of eccentricity found are remarkably small considering the simplicity of the method employed. Simulations with higher charge-to-mass ratio, especially in the case of opposite charges, may have a significant residual eccentricity. There are at least three ways to improve our method and further remove the eccentricity.

First, one can adapt iterative eccentricity-reduction schemes, such as those described in [100, 103, 104] for uncharged black holes, to systems with charge. Alternatively, one can use post-Newtonian methods that include directly electromagnetic fields to estimate the linear momenta. The two methods are not mutually exclusive, and for simulations with extreme charge both may be required to produce quasi-circular inspirals. Finally, one can always start the evolution from a larger initial separation and let gravitational and electromagnetic waves circularize the orbit.

### C. Achieving long-term stable evolutions

Performing long-term, stable evolutions of black holes in vacuum in 3+1 dimensions used to be the greatest challenge in numerical relativity. Through substantial developments over the past two decades, solving the Einstein equations in vacuum is considered a solved problem, and there is considerable knowledge on the topic. However, simulations of black holes with electromagnetic fields are still in their infancy. It is not yet clear how much of the technology developed for vacuum spacetimes carries over to electrovacuum spacetimes. Being able to perform long-term and stable evolutions of charged black holes is therefore not granted. Indeed, the simulations presented in this work are among the longest and most sophisticated to date, and presented some challenges. We found that adding artificial dissipation to all evolved variables in a specific way is critical for successful simulations. We found that standard recipes for artificial dissipation that work in the case of vacuum binary black hole spacetimes lead to blowups in the case of electrovacuum binary black holes.

Artificial dissipation stabilizes evolutions by removing high-frequency unstable modes. This approach has proven necessary to achieve long-term simulations in many cases (see, e.g. [105–111]). The most common flavor of artificial dissipation adopted in numerical relativity is known as *Kreiss-Oliger dissipation* [68]. This technique consists of introducing artificial diffusion by adding a term to the evolution equation of a variable $U$ as follows (schematically)

$$\partial_t U = \cdots + (-1)^{(p+3)/2} \frac{\epsilon}{2^{p+1}} \Delta x^p \partial_x^{p+1} U \,, \qquad (7)$$

where $\cdots$ indicate the right-hand-side of the evolution equation of $U$, $p$ is the order of the Kreiss-Oliger dissipation, $\Delta x$ is the grid spacing and the numerical factor $\epsilon \Delta x^p / 2^{p+1}$ is the diffusivity, which represents the strength of the dissipation. Note that although we only add a spatial derivative in the $x$ direction in Eq. (7), the actual operator has also corresponding $y$ and $z$ derivatives. For simplicity of the presentation we do not write these extra terms here. In the infinite resolution limit, this new term vanishes and the equations are the ones we started with. However, at finite resolution, it is important to ensure that the modification does not affect the convergence order of the solution. Thus, $p$ is typically chosen to be greater than the convergence order of the evolution operator. Moreover, $p$ has to be odd, so that this modification is an even-order parabolic operator (since $p+1$ is even). In Appendix A, we present some details on conditions that must be satisfied for numerical stability.

As in previous works, our simulations quickly crash (in the first $100\,M$) if we do not add artificial diffusion.

Since our evolutions are sixth-order accurate, we add a seventh-order ($p = 7$) dissipation to all evolved variables (i.e., including the spacetime and electromagnetic fields and the gauge variables). The strength of the dissipation is determined by the coefficient $\epsilon$ (see, Appendix A for details). We explored three prescriptions for setting $\epsilon$ on different refinement levels: (1) constant $\epsilon$, (2) proportional to the local Courant factor $\Delta t/\Delta x$, and (3) "continuous" $\epsilon$ (described below). The rationale behind (1) is to have a form that respects the local Courant stability condition independently of $\Delta x$ as long as the Courant factor is the same everywhere. It also has increased effective dissipation in regions with coarser resolution. Numerical stability requirements often require that different refinement levels be evolved with different Courant factors, so prescription (2) amends (1) by modifying $\epsilon$ when the Courant factor is changed to ensure that Courant stability conditions are met (see Appendix A). While (1) and (2) are commonly used in numerical relativity, (3) is introduced in this paper and consists of setting $\epsilon_i = \epsilon_n(\Delta x_i/\Delta x_n)^{-p}$, where $i = 1, 2, \ldots, n$ is the index indicating the refinement level (larger $i$ indicating finer level), with $n$ the maximum number of refinement levels, and $\Delta x_i$ the grid spacing of refinement level $i$. The above prescription can also be written as $\epsilon_i = \epsilon_0/(2^{i-n})^p$, since refinement level grid spacings differ by factors of 2, i.e., $\Delta x_{i-1} = 2\Delta x_i$. Thus, the diffusivity entering Eq. (7) for each level becomes $\epsilon_n(\Delta x_i/\Delta x_n)^{-p}\Delta x_i^p/2^{p+1} = \epsilon_n \Delta x_n^p/2^{p+1}$. In other words, this new prescription guarantees that the effective diffusivity is the same everywhere on the grid, ensuring that the same parabolic diffusion operator is added to the set of equations on each refinement level. Moreover, the artificial diffusion again goes to 0 at order $p$, and thus does not affect the expected order of convergence of the finite difference scheme. We call this *continuous*, because prescriptions (1) and (2) have jumps in the effective diffusivity across refinement levels that introduce discontinuities in the equations. Hence, the parabolic operator added to the equations depends on the refinement level, which results in effectively solving a different system of partial differential equations on different refinement levels. This difference vanishes in the limit of infinite resolution. To our knowledge our approach (3) for setting the Kreiss-Oliger diffusivity on adaptive-mesh-refinement grids has not been discussed before. We found that this is a crucial ingredient for long-term and stable numerical evolutions of charged black holes.

To demonstrate the performance of each of the three prescriptions for setting $\epsilon$, we consider a high-resolution simulation of a single charged, non-spinning black hole with mass $M = 1$ and charge $Q = 0.5\,M$. In Fig. 2, we show the L2 norm of the violation of the Hamiltonian constraint (excluding the domain interior to the apparent horizon) for each dissipation prescription. More details about our numerical setup are provided in Appendix B. The figure is representative of how our binary charged black hole simulations evolve, and demonstrates that there is unstable growth in some variables.[5] We verified that this instability is numerical and not physical, since its onset depends on the resolution of the simulation: the higher the resolution, the earlier the instability takes place. This behavior was not reported in previous studies without charge, suggesting that the instability first arises in the electromagnetic sector, and then feeds the gravitational one. Indeed, we observe the numerical instability starts first in electromagnetic quantities, such as the Gauss constraint. We also found that the unstable growth of the constraint first occurs near the outer boundary, suggesting that the approximate outgoing-wave boundary conditions may be the trigger of the instability. Finally, we noticed that a fourth-order accurate finite-difference evolution (with fifth order dissipation) and constant $\epsilon$ does not lead to the same numerical explosions at the same resolution and within the simulation times we considered. What is important to note regarding the goals of this paper is that prescription (3) allows us to perform long evolutions with constraints converging to zero when the resolution is increased when adopting sixth-order accurate finite differences. Studying the interplay between dissipation, convergence order of the numerical scheme, and boundary conditions is left for future works.

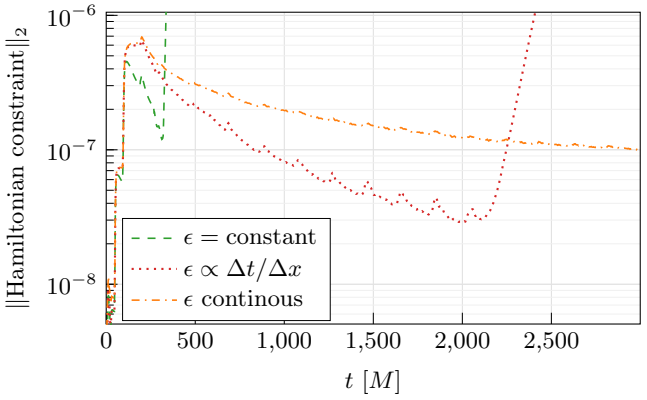


FIG. 2. Evolution of the L2 norm of the Hamiltonian constraint (outside the horizon) for the three different Kreiss-Oliger dissipation prescriptions. The "continuous" dissipation prescription introduced in this work is the only one that allows long-term and stable simulations with seventh-order Kreiss-Oliger dissipation and sixth-order accurate finite differences.

For completeness, in Appendix C, we report two formulations that we experimented with to further improve

[5] The jumps in the constraints at the beginning of the simulations are due to an initial pulse in the gauge variables propagating outwards from the center of the simulation. Every time this pulse crosses a refinement boundary, it is turned into constraint-violating modes through refinement level interpolations. This behavior in the constraints is well-known [112].

the stability of the evolutions but did not result in additional improvements.

### D. Contribution of the electromagnetic fields to the spin of a black hole

The quasi-isolated horizon formalism is widely used in numerical relativity to determine quasi-local physical properties (such as mass or angular momentum) of black holes [113, 114]. However, the majority of previous simulations focused on the case with gravitational fields only, and hence, electromagnetic contributions to black hole quasi-local properties have not been considered. In [1], we presented the code `QuasiLocalMeasuresEM`, an extended version of `QuasiLocalMeasures` that implements the formalism for the full Einstein-Maxwell theory [115]. The main differences with respect to the purely gravitational case are in the computation of the mass and the angular momentum of a black hole. The full formalism also provides a quasi-local way to compute the charge of a black hole. Here, we focus on spin (for a complete discussion, see Sec. II C in [1]).

While the expression for angular momentum at infinity does not depend on electromagnetic fields [116], the quasi-local formula does [115]. So, to compute the angular momentum $J$ of a charged black hole, one must calculate two terms: $J_{\rm GR}$ and $J_{\rm EM}$ (see, Sec. II C in [1] for more details). The computation of $J_{\rm GR}$ is implemented in the `QuasiLocalMeasures` thorn of the `Einstein Toolkit`. `QuasiLocalMeasuresEM` computes $J_{\rm EM}$ as well. We find that this contribution can be a significant fraction on the total spin. In Fig. 3, we show the ratio between $J_{\rm EM}$ and the total angular momentum of the remnant black hole forming in our binary simulations $J^{\rm final}_{\rm EM}/J^{\rm final}$ for the various simulations in our set. The maximum value in our simulations is with $\lambda^+_+ = 0.3$, where we find that $J^{\rm final}_{\rm EM}/J^{\rm final} \approx 3.8\,\%$. Fig. 3 shows that this ratio depends quadratically on the charge-to-mass ratio of the final black hole. A fit confirms quantitatively that this is the case.

`TwoChargedPunctures` always generates (binary) black hole initial data with $J_{\rm EM} = 0$, because of the choice of the initial electromagnetic fields [1]. Soon after the evolution starts, the initial data relax to a non-zero $J_{\rm EM}$ on a few light-crossing times while keeping the total angular momentum constant. In Fig. 4, we show how the two contributions to the spin behave for the case of a highly charged, rapidly spinning black hole with $Q = 0.6\,M$ and $J = 0.6\,M^2$. In this case, after the initial data relax $J^{\rm final}_{\rm EM}/J^{\rm final}$ is approximately 11 %. Monitoring this quantity also provides a way to quantify when the initial data has relaxed.

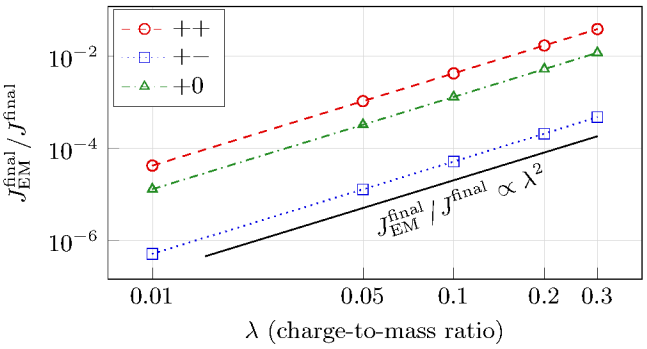


FIG. 3. Contribution of the electromagnetic fields to the spin of the final black hole. The relative importance of the spin due to electromagnetic fields $J_{\rm EM}$ scales as the charge-to-mass ratio squared. For details of the formalism, see Sec. II C in [1].

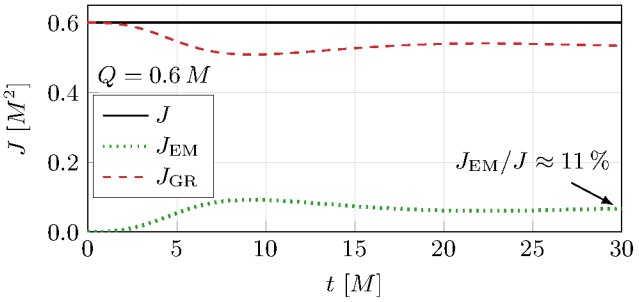


FIG. 4. Various contributions to the angular momentum of a rapidly spinning and highly charged black hole with $J = 0.6\,M^2$ and $Q = 0.6\,M$. As a result of the choice of the initial electromagnetic fields, `TwoChargedPunctures` [1] generates initial data with $J_{\rm EM} = 0$. During the evolution, the initial data relax to a non-zero $J_{\rm EM}$ while $J$ remains conserved.

### E. Wave extraction

We adopt the Newman-Penrose formalism [117] with the same conventions as in [23] to extract gravitational and electromagnetic waves from our simulations. In this subsection, we review the formalism with focus on the electromagnetic sector. The Newman-Penrose formalism of the gravitational sector is a standard topic in the literature (e.g. [81, 118, 119]). Details on the numerical implementation of the calculation of the various quantities presented below can be found in [23] and [120].

We consider a null tetrad of complex vectors $k^a, l^a, m^a$ and $m^{*a}$ with null mutual inner products except for $-k^a l_a = 1 = m^a m^*_a$. We also define the Newman-Penrose scalars constructed with the Faraday tensor [121]

$$\Phi_0 = F_{ab} l^a m^b \,, \tag{8a}$$

$$\Phi_1 = \frac{1}{2} F_{ab} (l^a k^b + m^{*a} m^b) \,, \tag{8b}$$

$$\Phi_2 = F_{ab} m^{*a} k^b \,. \tag{8c}$$

Appendix D connects $\Phi_0$, $\Phi_1$ and $\Phi_2$ with the electric and

magnetic fields in flat spacetime and provides physical arguments to build intuition on what the different scalars represent.

In asymptotically flat spacetimes, the Newman-Penrose scalars have a known fall-off behavior at large spatial distances (the so-called "peeling theorem" [122])

$$\Phi_0 \sim \frac{1}{r^3}\,, \qquad \Phi_1 \sim \frac{1}{r^2}\,, \qquad \Phi_2 \sim \frac{1}{r}\,, \tag{9}$$

where the $\sim$ indicates the asymptotic behavior as $r \to \infty$. We will use these properties to find which terms are important for computations at infinity and which are not.

By use of Eqs. (8), we can express the electromagnetic field tensor as

$$\begin{aligned} F_{ab} = 2\Big[&\Phi_1(k_{[a}l_{b]} + m_{[a}m^*_{b]}) + \Phi_2 l_{[a}m_{b]} + \Phi_0 m^*_{[a}k_{b]}\Big] \\ &+ \text{complex conjugate}\,, \end{aligned} \tag{10}$$

where "complex conjugate" refers to the term in square brackets, and square brackets next to indices imply anti-symmetrization. Considering the electromagnetic stress-energy tensor

$$4\pi T^{\rm EM}_{ab} = F_{ac}F_{bd}g^{cd} - \frac{1}{4}g_{ab}F_{cd}F^{cd}\,, \tag{11}$$

we can express this in terms of the Newman-Penrose scalars [121]

$$\begin{aligned} 4\pi T^{\rm EM}_{ab} = &\Big[\Phi_0\Phi_0^* k_a k_b + 2\Phi_1\Phi_1^*\left(l_{(a}k_{b)} + m_{(a}m^*_{b)}\right) \\ &+ \Phi_2\Phi_2^* l_a l_b - 4\Phi_0^*\Phi_1 k_{(a}m_{b)} \\ &- 4\Phi_1^*\Phi_2 l_{(a}m_{b)} + 2\Phi_2\Phi_0^* m_a m_b\Big] \\ &+ \text{complex conjugate}\,, \end{aligned} \tag{12}$$

where the complex conjugate is of the term in square brackets.

Assuming asymptotically spherical coordinates $(r, \theta, \varphi)$ centered on the Cartesian grid and oriented along the $z$ direction and $t$ along the normal to the hypersurfaces, we can choose as null tetrad

$$k^a = \frac{1}{\sqrt{2}}(e^a_{\hat{t}} - e^a_{\hat{r}})\,, \tag{13a}$$

$$l^a = \frac{1}{\sqrt{2}}(e^a_{\hat{t}} + e^a_{\hat{r}})\,, \tag{13b}$$

$$m^a = \frac{1}{\sqrt{2}}(e^a_{\hat{\theta}} + ie^a_{\hat{\varphi}})\,, \tag{13c}$$

$$m^{*a} = \frac{1}{\sqrt{2}}(e^a_{\hat{\theta}} - ie^a_{\hat{\varphi}})\,, \tag{13d}$$

with $\boldsymbol{e}_{\hat{t}}, \boldsymbol{e}_{\hat{r}}, \boldsymbol{e}_{\hat{\theta}}, \boldsymbol{e}_{\hat{\phi}}$ orthonormal non-coordinate basis. Note that in the coordinate basis, it holds that $m_a \sim r$.

The energy and angular momentum fluxes per solid angle carried away by outgoing electromagnetic waves at infinity is given by

$$\frac{\mathrm{d}^2E}{\mathrm{d}t\,\mathrm{d}\Omega} = \lim_{r\to+\infty} r^2 T^r{}_t\,, \tag{14a}$$

$$\frac{\mathrm{d}^2L^z}{\mathrm{d}t\,\mathrm{d}\Omega} = \lim_{r\to+\infty} r^2 T^r{}_\varphi\,. \tag{14b}$$

Here we focus on the $z$ component of the angular momentum. These quantities can be expressed in terms of the Newman-Penrose scalars by use of Eqs. (9) and (12). The only non-zero contribution to the energy flux arises from the term $|\Phi_2|^2 l_t l_r/2\pi$. Hence,

$$\frac{\mathrm{d}^2E}{\mathrm{d}t\,\mathrm{d}\Omega} = \lim_{r\to+\infty} r^2 T^r{}_t = \lim_{r\to+\infty}\frac{r^2}{2\pi}|\Phi_2|^2\,. \tag{15}$$

Considering the fall-off behavior of the Newman-Penrose scalars in Eqs. (9), the angular momentum flux becomes

$$\lim_{r\to+\infty} r^2 T^r{}_\varphi = \lim_{r\to+\infty} -\frac{r^2}{2\pi}\left(\Phi_1^*\Phi_2 l_r m_\varphi + \Phi_1\Phi_2^* l_r m^*_\varphi\right)\,, \tag{16}$$

which can be rewritten as

$$\begin{aligned} \lim_{r\to+\infty} r^2 T^r{}_\varphi &= \lim_{r\to+\infty} -\frac{r^2}{4\pi}\left(\Phi_1^*\Phi_2 ir\sin\theta - \Phi_1\Phi_2^* ir\sin\theta\right) \\ &= \lim_{r\to+\infty} -\frac{ir^3\sin\theta}{4\pi}\left(\Phi_1^*\Phi_2 - \Phi_1\Phi_2^*\right) \\ &= \lim_{r\to+\infty} \frac{r^3\sin\theta\Im[\Phi_1^*\Phi_2]}{2\pi}\,, \end{aligned}$$

where $\Im[z]$ is the imaginary part of the complex number $z$. Therefore, the flux of angular momentum that crosses a sphere at large radius $r$ is

$$\frac{\mathrm{d}^2L^z}{\mathrm{d}t\,\mathrm{d}\Omega} = \frac{1}{2\pi}r^3\sin\theta\Im[\Phi_1\Phi_2^*]\,. \tag{17}$$

Here we reach the same conclusion as in [123]: the flux of angular momentum does not depend only on the radiative degrees of freedom (encoded in $\Phi_2$), but there is also a Coulombic contribution (encoded in $\Phi_1$) [124]. This is a striking difference compared to gravitational waves, for which the information contained in the radiative degrees of freedom, i.e. $\Psi_4$, is sufficient for computing the flux of angular momentum [125].

We perform a decomposition in spin-weighted spherical harmonics $Y^s_{\ell m}$ with spin $s = -2, -1, 0$

$$\Phi_1(r,\theta,\varphi) = \sum_{\ell\geq 0}\sum_{-\ell\leq m\leq\ell}\phi_1^{\ell m}Y^0_{\ell m}\,, \tag{18a}$$

$$\Phi_2(r,\theta,\varphi) = \sum_{\ell\geq 1}\sum_{-\ell\leq m\leq\ell}\phi_2^{\ell m}Y^{-1}_{\ell m}\,, \tag{18b}$$

$$\Psi_4(r,\theta,\varphi) = \sum_{\ell\geq 2}\sum_{-\ell\leq m\leq\ell}\psi_4^{\ell m}Y^{-2}_{\ell m}\,. \tag{18c}$$

Using the orthogonality relations between spin-weighted spherical harmonics with the same spin, we can write [80]

$$\frac{\mathrm{d}E_{\rm EM}}{\mathrm{d}t} = \lim_{r\to+\infty}\frac{r^2}{4\pi}\sum_{\ell,m}|\phi_2^{\ell m}|^2\,, \tag{19a}$$

$$\frac{\mathrm{d}E_{\rm GW}}{\mathrm{d}t} = \lim_{r\to+\infty}\frac{r^2}{16\pi}\sum_{\ell,m}\left|\int_{-\infty}^{t}\mathrm{d}t'\psi_4^{\ell m}\right|^2\,, \tag{19b}$$

$$\frac{\mathrm{d}L_{\rm GW}}{\mathrm{d}t} = \lim_{r\to+\infty}\frac{r^2}{16\pi}\sum_{\ell,m} m\Im\left[\left(\int_{-\infty}^{t}\mathrm{d}t'\psi_4^{\ell m}\right)\right. \tag{19c}$$
$$\left.\times\left(\int_{-\infty}^{t}\mathrm{d}t'\int_{-\infty}^{t'}\mathrm{d}t''\psi_4^{\ell,m*}\right)\right]\,.$$

The sums on $m$ go from $-l$ to $l$. In practice, we truncate the expansion to $l = 8$ and we use a finite extraction radius. There is no simple relation between the angular momentum lost by electromagnetic waves and the multipolar components $\phi_2^{\ell m}$ and $\phi_1^{\ell m}$ when decomposed with the respective spin-weight, so we implemented directly Eq. (17). We tested this new diagnostic for the flux of angular momentum against the analytical Michel solution [126, 127] (see, Appendix E).

## III. QUADRUPOLE APPROXIMATION MODEL

The simplest waveform model for charged binary black holes is obtained from the Keplerian motion of charged massive particles in Newtonian physics with the inclusion of radiation reaction. We indicate this model with the initials QA (*quadrupole approximation*). We will also refer to it as the "Newtonian model".

Let us consider two point particles with masses $m_1$, $m_2$ and charges $q_1$, $q_2$ on a circular orbit at separation $d$. The total energy (kinetic + gravitational + electrostatic) of the system $E$ is

$$E = -\frac{m_1 m_2}{2d} - \frac{q_1 q_2}{2d} = -(1-\lambda_1\lambda_2)\frac{m_1 m_2}{2d}\,, \tag{20}$$

where $\lambda_i = q_i/m_i$ is the charge-to-mass ratio of the $i$-th particle.

The system loses energy by emission of gravitational and electromagnetic waves. In this work, we will restrict to circular orbits and only consider dipole and quadrupole electromagnetic waves, and quadrupole gravitational waves [36, 47]

$$\frac{\mathrm{d}E_{\rm EM}^{\rm dip}}{\mathrm{d}t} = \frac{2}{3}(\lambda_1-\lambda_2)^2(1-\lambda_1\lambda_2)^2\frac{m_1^2 m_2^2}{d^4}\,, \tag{21a}$$

$$\frac{\mathrm{d}E_{\rm GW}^{\rm quad}}{\mathrm{d}t} = \frac{32}{5}(1-\lambda_1\lambda_2)^3\frac{m_1^2 m_2^2 M}{d^5}\,, \tag{21b}$$

$$\frac{\mathrm{d}E_{\rm EM}^{\rm quad}}{\mathrm{d}t} = \left(\frac{m_2\lambda_1}{2M}+\frac{m_1\lambda_2}{2M}\right)^2\frac{\mathrm{d}E_{\rm GW}^{\rm quad}}{\mathrm{d}t}\,. \tag{21c}$$

This can be extended to eccentric orbits [47]. The angular momentum carried away by gravitational and electromagnetic waves in the dipole and quadrupolar channels is given by [47]

$$\frac{\mathrm{d}J_{\rm EM}^{\rm dip}}{\mathrm{d}t} = \frac{\mathrm{d}E_{\rm EM}^{\rm dip}}{\mathrm{d}t}\Big/\sqrt{(1-\lambda_1\lambda_2)\frac{M}{d^3}}\,, \tag{22a}$$

$$\frac{\mathrm{d}J_{\rm GW}^{\rm quad}}{\mathrm{d}t} = \frac{\mathrm{d}E_{\rm GW}^{\rm quad}}{\mathrm{d}t}\Big/\sqrt{(1-\lambda_1\lambda_2)\frac{M}{d^3}}\,. \tag{22b}$$

Note that the denominator is the orbital angular velocity of the binary.

We can derive the equation of motion by taking the derivative of Eq. (20) and applying the chain rule

$$\frac{\mathrm{d}E}{\mathrm{d}t} = (1-\lambda_1\lambda_2)\frac{m_1 m_2}{2d^2}\frac{\mathrm{d}d}{\mathrm{d}t}\,. \tag{23}$$

Therefore,

$$\frac{\mathrm{d}d}{\mathrm{d}t} = \frac{2d^2}{(1-\lambda_1\lambda_2)m_1 m_2}\frac{\mathrm{d}E}{\mathrm{d}t}\,. \tag{24}$$

To respect energy conservation, $\mathrm{d}E/\mathrm{d}t$ is given by the total energy loss via electromagnetic and gravitational radiation provided by Eqs. (21a), (21b), (21c). The resulting equation of motion (24) cannot be solved analytically in closed form for a non-zero charge. Here, we solve it numerically with the LSODA solver [128] of ODEPACK [129] through the SciPy interface [130]. The time integration is performed with a timestep that is proportional to the orbital separation. We continue the integration up to $d = 5\,M$, which is an average radius of the Innermost Stable Circular Orbit (ISCO) for neutral particles around Kerr-Newman black holes (more on this in Sec. IV A).

The solution of Eq. (24) provides the time evolution of the orbital separation. Then, using Eqs. (21), (22), we can compute the energy and angular momentum lost by gravitational and electromagnetic waves. We can also compute the gravitational-wave strain in the quadrupole approximation [70, 131] measured at distance $r$ from the binary

$$rh_+ = 4(1-\lambda_1\lambda_2)^{\frac{5}{3}}\frac{m_1 m_2}{M^{\frac{1}{3}}}(\pi f_{\rm GW})^{\frac{2}{3}}\cos\phi_{\rm GW}\,, \tag{25a}$$

$$rh_\times = 4(1-\lambda_1\lambda_2)^{\frac{5}{3}}\frac{m_1 m_2}{M^{\frac{1}{3}}}(\pi f_{\rm GW})^{\frac{2}{3}}\sin\phi_{\rm GW}\,. \tag{25b}$$

The frequency of the gravitational waves $f_{\rm GW}$ is twice the orbital frequency,

$$f_{\rm GW}(d) = \frac{1}{\pi}\sqrt{\frac{(1-\lambda_1\lambda_2)M}{d^3}}\,. \tag{26}$$

Defining $\omega_{\rm GW}(d) = 2\pi f_{\rm GW}(d)$, the phase of the gravitational waves $\phi_{\rm GW}$ is

$$\phi_{\rm GW} = \phi_0 + \int_{d_0}^{d}\frac{\omega_{\rm GW}(R)}{\dot{d}(R)}\,\mathrm{d}R\,, \tag{27}$$

where $\phi_0$ is an arbitrary initial phase and $\dot{d}(R)$ is the time derivative of $d$ evaluated at orbital separation $R$, which can be computed from Eq. (24).

Finally, we note that the computational requirements of the QA model are negligible compared to numerical-relativity simulations (as Eq. (24) is a single ordinary differential equation). In certain limits, the equations can be even solved analytically [36].

## IV. THE REMNANT BLACK HOLE

The properties of the remnant black hole that forms following a binary black hole merger are key to testing general relativity [73, 132, 133]. Perturbation theory applies to the post-merger black hole, and it is well established that perturbed black holes settle by undergoing characteristic damped oscillations. This is known as quasi-normal-mode ringing. In general relativity, the complex frequency of these oscillations is completely determined by the black hole mass, spin, and charge.

In this section, we first present the details of an existing method to estimate the spin of the remnant black hole forming following mergers of charged black holes. Next, we discuss quasi-normal-modes. The two discussions are closely related as the quasi-normal-modes depend on the properties of the black hole.[6]

For the values of charge-to-mass ratios $\lambda$ considered in this work, the quasi-normal-modes are primarily determined by the spin of the final black hole, because $\lambda$ is not large enough to matter. However, the final spin depends on the charge of the binary components. Even when the total charge is zero, e.g. the two black holes have equal and opposite charges, the final spin is expected to be different from the uncharged case, allowing, in principle, to distinguish the two scenarios.

### A. Remnant black hole spin model

A simple way to estimate the spin of the remnant black hole forming following the merger of two black holes on a quasi-circular orbit is to invoke conservation arguments (this method is sometimes known with the acronym BKL [137], from the names of the authors). The approach aims to be 10 % accurate [137], and while it was first applied to Kerr-Newman black holes in [74], the performance of the approximation has not been tested in the case of charged black hole inspirals. Therefore, it is unknown if the accuracy goal is met for more generic cases. Here we use our quasi-circular inspiral calculations to gauge the accuracy of the BKL approach.

The basic assumption of the method is that during an inspiral the black-hole orbital separation shrinks due emission of gravitational waves until the ISCO is reached, at which point the two black holes plunge. During the plunge, little angular momentum is lost, so one can estimate the spin of the remnant black hole by studying the ISCO.

Consider the merger of two non-spinning black holes with mass $m_1$, $m_2$ and charge $q_1$, $q_2$. The total mass and charge of the system are

$$M = m_1 + m_2\,, \quad Q = q_1 + q_2\,. \tag{28}$$

Given that the energy lost via gravitational waves is of order of a few percent of $M$ (smaller than the target accuracy of 10 %), the BKL method assumes that the total mass is conserved. Therefore, the final black hole has mass $M$. Attempts to include energy loss in the uncharged case were made [138], but we will not consider this here. Charge is exactly conserved, so the final black hole must have charge $Q$. To determine the remnant black hole spin parameter $a$, one invokes angular momentum conservation. The BKL model postulates that the final angular momentum $Ma$ is exactly the same as the orbital angular momentum at the onset of the plunge. This quantity is then estimated by considering the motion in the spacetime of the remnant black hole of a test particle with mass $\mu$ and charge $q$ given by

$$\mu = \frac{m_1 m_2}{M}\,, \quad q = \frac{q_1 q_2}{Q}\,, \tag{29}$$

where $\mu$ and $q$ are the reduced mass and charge of the binary system (namely, the mass and charge of the equivalent effective one-body problem).

Let $L_{M,a,Q}$ be the ISCO angular momentum of a test particle with mass $\mu$ and charge $q$ in a Kerr-Newman spacetime with mass $M$, spin $a$, and charge $Q$, then the BKL approach sets

$$Ma = L_{M,a,Q}(r_{\rm ISCO})\,. \tag{30}$$

If $l = L_{M,a,Q}(r_{\rm ISCO})/\mu$ is the test particle specific angular momentum, then we have

$$a = \nu l_{M,a,Q}(r_{\rm ISCO})\,, \tag{31}$$

where $\nu = \mu/M = (m_1 m_2)/M^2$ is the symmetric mass ratio. Equation (31) determines the spin $a$ of the final black hole. It is straightforward to extend the method to consider spinning binaries by adding the contribution of the individual spins to the total angular momentum in Eq. (30), but we will not do this here, because our numerical relativity simulations of charged binaries do not involve spin.

To solve Eq. (31), we need to compute the specific angular momentum of the test particle with charge $q$ in a circular orbit at radius $r_{\rm ISCO}$. We do this in the standard way by defining an effective radial potential $V_{\rm eff}(r)$.

In Boyer-Lindquist coordinates $(t, r, \theta, \phi)$, the line element $\mathrm{d}s^2$ of a Kerr-Newman black hole with mass $M$,

[6] Another way in which the two discussions are linked is that the study of geodesic motion can be used to estimate the quasi-normal-mode frequencies from the light-ring properties [134–136].

spin $a$, and charge $Q$ is given by [139, 140]

$$\begin{aligned} \mathrm{d}s^2 = &-\frac{\Delta - a^2\sin^2\theta}{\rho^2}\,\mathrm{d}t^2 + \frac{\rho^2}{\Delta}\,\mathrm{d}r^2 + \rho^2\,\mathrm{d}\theta^2 \\ &- 2a\sin^2\theta\frac{(r^2+a^2-\Delta)}{\rho^2}\,\mathrm{d}t\,\mathrm{d}\phi \\ &+ \frac{(r^2+a^2)^2 - \Delta a^2\sin^2\theta}{\rho^2}\sin^2\theta\,\mathrm{d}\phi^2\,, \end{aligned} \tag{32}$$

with

$$\rho^2 = r^2 + a^2\cos^2\theta\,, \tag{33a}$$

$$\Delta = r^2 - 2Mr + a^2 + Q^2\,. \tag{33b}$$

The electromagnetic vector potential is

$$A = -\frac{Qr}{\rho^2}(\mathrm{d}t - a\sin^2\theta\,\mathrm{d}\phi)\,. \tag{34}$$

For Kerr-Newman black holes, $V_{\rm eff}$ is given by [74, 141]

$$V_{\rm eff} = \frac{g_{tt}\tilde{l}^2 + 2g_{t\phi}\tilde{l}\tilde{\varepsilon} + g_{\phi\phi}\tilde{\varepsilon}^2 - \Delta}{g_{rr}\Delta}\,, \tag{35}$$

with

$$\tilde{l} = l + qA_\phi\,, \tag{36a}$$

$$\tilde{\varepsilon} = \varepsilon - qA_t\,, \tag{36b}$$

where $\varepsilon$ and $l$ are the specific energy and specific angular momentum, respectively. The properties of the ISCO are found solving the following equations simultaneously

$$V_{\rm eff}(r_{\rm ISCO}) = 0\,, \tag{37a}$$

$$\frac{\mathrm{d}V_{\rm eff}}{\mathrm{d}r}(r_{\rm ISCO}) = 0\,, \tag{37b}$$

$$\frac{\mathrm{d}^2V_{\rm eff}}{\mathrm{d}r^2}(r_{\rm ISCO}) = 0\,. \tag{37c}$$

for $r_{\rm ISCO}$, $\varepsilon(r_{\rm ISCO})$ and $l(r_{\rm ISCO})$.

For the estimate of the spin, we are particularly interested in $l(r_{\rm ISCO})$. Once that is known, we use a root-finding method to solve numerically Eq. (30) and find the spin of the final black hole.

### B. Quasi-normal-modes

Following merger, the remnant black hole settles by undergoing quasi-normal mode ringing, i.e., damped oscillations with specific frequencies $\omega$ and decay times $\tau$ [142].[7] During the ringdown phase, the Newman-Penrose scalar $\Psi_4$ looks like

$$\Psi_4(t,r) \sim \sum_{\ell mn} A_{\ell m}(r)\mathrm{e}^{-t/\tau_{\ell mn}}\sin(\omega_{\ell mn}t)\,, \tag{38}$$

with $l$, $m$ being the multipolar mode numbers and $n$ the overtone number; $A, \tau$, and $\omega$ are the characteristic amplitude, the decay time, and the frequencies of the quasi-normal modes. These values depend on the mass, spin, and charge of the black hole in a known way [73, 133]. In this work, we are interested in exploring the charge information contained in the ringdown waveforms. In particular, we test whether it is possible to tell whether a merging binary had charge by looking at the post-merger signal alone.

For Schwarzschild and Kerr black holes, the values of $\omega_{\ell mn}$ and $\tau_{\ell mn}$ are tabulated [143, 144] or available in public codes, like the one we use here–`qnm` [145]. For generic Kerr-Newman solutions, while the problem has been solved [146], such tables are not publicly available. However, since the simulations in our set have relatively small charge-to-mass ratio, we can work in the small charge limit and we can use the equations provided in [44] for the $\ell = 2$, $m = 2$, $n = 0$ quasi-normal mode (which typically dominates [147, 148]). As shown in [44], for a Kerr-Newman black hole with charge-to-mass ratio $\lambda$ and dimensionless spin $\chi$, the first correction to $\omega_{220}$ and $\tau_{220}$ with respect to the uncharged values $\omega_{220}^{\lambda=0}$ and $\tau_{220}^{\lambda=0}$ is:

$$\frac{\delta\omega_{220}}{\omega_{220}^{\lambda=0}} = \lambda^2\left[-0.2812 - 0.0243\chi + \frac{0.3506}{(1-\chi)^{0.505}}\right]\,, \tag{39a}$$

$$\begin{aligned} \frac{\delta\tau_{220}}{\tau_{220}^{\lambda=0}} = -\lambda^2\Bigg[&0.1075 + 0.089\,23\chi + 0.023\,14\chi^2 \\ &+0.094\,43\chi^3 - \frac{0.075\,85}{(1-\chi)^{1.2716}}\Bigg]\,, \end{aligned} \tag{39b}$$

with $\delta\omega_{220} = \omega_{220} - \omega_{220}^{\lambda=0}$ and $\delta\tau_{220} = \tau_{220} - \tau_{220}^{\lambda=0}$. In this work, we use `qnm` [145] to compute $\omega_{220}^{\lambda=0}$ and $\tau_{220}^{\lambda=0}$ and Eqs. (39) to compute the quasi-normal modes for our charged remnants.

We can plug a representative remnant black hole spin value $\chi = 0.67$ in Eq. (39) to gain some insight on the effect of charge, which yields $\delta\omega_{220}/\omega_{220}^{\lambda=0} \approx \lambda^2/3$, and $\delta\tau_{220}/\tau_{220}^{\lambda=0} \approx \lambda^2/10$. For the values of $\lambda$ treated in our simulations, if we assumed that all black holes had the same final mass and spin, then the deviations from the Kerr quasi-normal modes are at most at the percent level. The deviations are maximized for larger $\lambda$, so one would expect that the simulation with $\lambda_+^+$ is the easiest to constrain. However, if one wanted to tackle the question "Can we tell from the ringdown if the binary was charged?" the problem is more complicated and one needs to consider the interplay between mass, spin, and charge. We discuss this in Sec. V C 2.

## V. SIMULATION RESULTS AND DISCUSSION

In this section, we describe the results from our black hole binary simulations through the inspiral, merger and

[7] Here we are considering relatively small charge, so we will only be focusing on the gravitational quasi-normal-modes.

ringdown phases. We start by analyzing the inspiral (Sec. V A). We compare the non-linear solutions with the QA model, finding that the Newtonian approach always overestimates observable quantities by 20–100 %. Next, we present our numerical-relativity simulations up to merger (Sec. V B), discussing properties of the emission (Sec. V B 1) and detectability of charge by future gravitational wave observatories (Sec. V B 2). Finally, we explore the ringdown phase (Sec. V C), testing the BKL approach (Sec. V C 1) and discussing quasi-normal-modes (Sec. V C 2).

### A. Inspiral

Here, we focus on the inspiral part of our calculations and we assess the performance of the Newtonian model within the quadrupole approximation (QA). Since high-order PN and/or effective-one-body waveforms including electromagnetic fields are not yet available, this model is the most widely used to study inspirals of charged black holes (e.g. [36, 44, 47–49, 70, 71]).

To compare numerical-relativity simulations with the Newtonian model, we consider a set of quantities of interest. To keep our results gauge-independent, we analyze these quantities between reference gravitational-wave frequencies $f_0, f_1$, and $f_2$, which we choose as follows: $Mf_0 = 9.61\times10^{-3}$, $Mf_1 = 1.76\times10^{-2}$, and $Mf_3 = 3.84\times10^{-2}$, where $M$ is the detector-frame ADM mass. The frequency $Mf_0$ corresponds to approximately 28 Hz for a binary with source-frame ADM mass $65\,M_\odot$ (detector-frame mass of approximately $70.6\,M_\odot$). These three frequencies are motivated by the LIGO sensitivity band with $f_0$ corresponding to the onset of the latest stage of the inspiral, $f_1$ to the intermediate phase prior to plunge, and $f_2$ to the plunge. Previous studies used the Newtonian model for LIGO-Virgo mergers, so our analysis here gauges how this approximate method performs and allows us to estimate the level of its accuracy. Since our numerical-relativity simulations scale with the total mass of the system $M$, we can target both stellar-mass and supermassive black hole binaries. In Table I we show what frequencies correspond to our reference frequencies $f_0, f_1, f_2$ for different choices of $M$. The table shows that this work is relevant to LIGO-Virgo as well as LISA sources [72]. In Sec. V B 2, we discuss charge detectability by LISA.

We designate by $t_f$ the coordinate time at which the gravitational-wave frequency is $f$, and using our non-linear simulations we compute the error of the QA model in gauge invariant quantities within the time intervals $[t_{f_0}, t_{f_1}]$ and $[t_{f_0}, t_{f_2}]$. The quantities we consider are: gravitational-wave phase, energy and angular momentum lost through emission, number of gravitational-wave cycles $N_{\rm GW}$, and the signal-to-noise ratio (SNR) between $f_{\rm min}$ and $f_{\rm max}$ (which are of particular interest to estimate charge detectability [44]). The latter two quantities

TABLE I. Reference frequencies $Mf_0 = 9.61\times10^{-3}$, $Mf_1 = 1.76\times10^{-2}$, and $Mf_3 = 3.84\times10^{-2}$ for different values of the detector-frame mass $M$. This study targets both LIGO-Virgo and LISA sources. The choice of $M = 70.6\,M_\odot$ is inspired by GW150914 [69]. The evolution from $f_0$ to $f_1$ is still not in the most relativistic part of the inspiral. On the other hand, $f_2$ is reached in the latest stages of the merger, following which the black holes plunge.

| Freq. | $M = 30\,M_\odot$ | $M = 70.6\,M_\odot$ | $M = 10^4\,M_\odot$ | $M = 10^7\,M_\odot$ |
|---|---|---|---|---|
| $f_0$ | 65 Hz | 28 Hz | 0.195 Hz | 0.195 mHz |
| $f_1$ | 120 Hz | 51 Hz | 0.357 Hz | 0.357 mHz |
| $f_2$ | 260 Hz | 111 Hz | 0.780 Hz | 0.780 mHz |

are computed as (see e.g., [131, 149])

$$N_{\rm GW} = \int_{f_{\rm min}}^{f_{\rm max}} \frac{f_{\rm GW}}{\dot f_{\rm GW}}\,{\rm d}f_{\rm GW}\,, \tag{40a}$$

$$\mathrm{SNR}^2 = 4\int_{f_{\rm min}}^{f_{\rm max}} \frac{|\tilde h(f)|^2}{S_n(f)}\,{\rm d}f\,, \tag{40b}$$

with $\tilde h$ Fourier transform of the strain and $S_n(f)$ the power spectral noise density of the detector. In the rest of the discussion, we focus on advanced LIGO at design sensitivity.

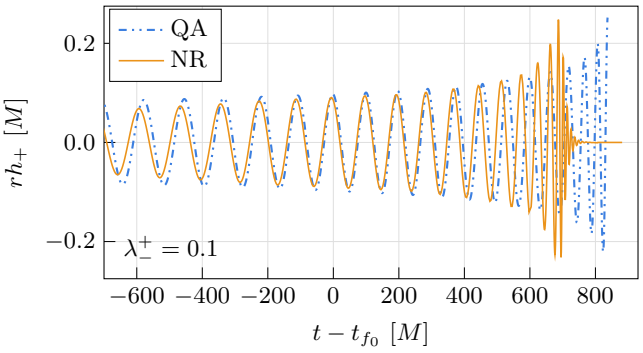


FIG. 5. Plus polarization of the gravitational-wave strain produced by oppositely charged binary black holes with $\lambda_-^+ = 0.1$ as extracted from the Newtonian (QA, blue, dash-dotted line) and full numerical-relativity simulation (NR, orange, solid line). The two waveforms are aligned a $t_{f_0}$, which is when the gravitational wave frequency is $f_0 = 9.61\times10^{-3}\,M^{-1}$. The main difference is that the fully relativistic simulations predict a faster merger, as they include all non-linear terms.

Before discussing the quantitative differences between the numerical relativity (NR) and QA models, we first provide a qualitative description. Figure 5 shows the plus polarization of the $\ell = 2$, $m = 2$ mode obtained with NR and the Newtonian model for a representative charge black hole binary with $\lambda_-^+ = 0.1$. The two waveforms shown in the figure are aligned at $t_{f_0}$, when they both have the same gravitational-wave frequency $f_0$. As the plot demonstrates, the QA model provides a decent approximation to the NR signal up to $t - t_{f_0} \approx 400\,M$. Shortly after that time, the black holes merge in the NR

simulation. Merger is never captured in the QA model, and the Newtonian simulation is stopped when the separation is of order of the ISCO (as in [70]). Also, there is substantial de-phasing before the frequency-alignment time. A major difference between the two models is that the relativistic simulation predicts a faster merger, because it includes all non-linear terms. As we will discuss later, this is the fundamental reason why the QA model overestimates all the interesting physical quantities.

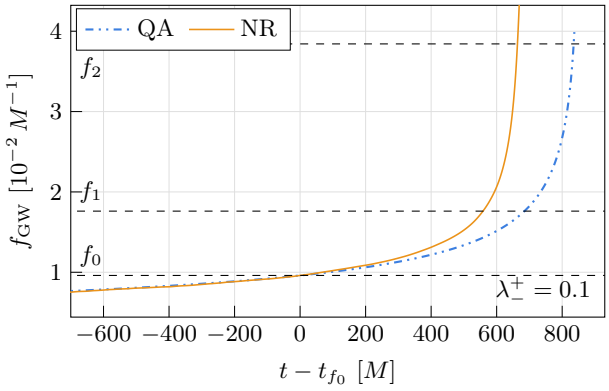


FIG. 6. Gravitational-wave frequency evolution for the Newtonian model and for the fully general-relativistic simulation. The two simulations are aligned at $t_{f_0}$, when the gravitational-wave frequency is $f_0$. Table I reports the values of $f_0, f_1$ and $f_2$.

We further emphasize this point in Fig. 6, where we report the frequency of the gravitational waves in the two models as a function of time. It is clear that the frequency evolves faster in the non-linear calculation. As a result, the QA computations spend more time inspiraling, so this model overestimates all relevant quantities, as it overestimates the time from $t_{f_0}$ to $t_{f_1}$ and $t_{f_2}$. This is exactly what happens at the quantitative level, too. Table II reports the relative error of the Newtonian calculations with respect to the NR simulations. For each quantity $\Upsilon$, the error is computed as

$$\text{relative error} = \frac{\Upsilon^{\rm QA} - \Upsilon^{\rm NR}}{\Upsilon^{\rm NR}} \,. \tag{41}$$

No absolute value is taken: a positive error means that the Newtonian approximation overestimates $\Upsilon$. The ranges of error reported are across all NR simulations we performed for this work. As the values in the table demonstrate, the listed quantities are always overestimated by order 20 % or more. However, we note that the QA model always captures the correct order of magnitude in the amplitude up until a couple of cycles prior to peak gravitational wave amplitude in the non-linear calculations. Hence, for the values of $\lambda$ considered here, the model can be used for rough estimates.[8]

[8] In [150, 151] it was shown that when adopting the quadrupole formula to estimate gravitational waves, but with the fluid distribution computed based on general relativistic simulations, the errors are of order 20 % in the amplitude. Here, we show the performance of the quadrupole approximation when not coupled to trajectories from numerical relativity simulations is significantly worse.

## B. Up to merger

Our simulations capture all non-linear effects that take place during the late inspiral and merger. So, we can study interesting quantities that are not accessible with approximate methods. In Fig. 7, we show the coordinate distance of the two black hole centroids as a function of the coordinate time for four representative NR simulations. This figure complements the top panel of Fig. 1. It can be seen that our Newtonian expectations are met: the system that merges faster is the one with opposite charge, due to the additional electrostatic attraction and loss of energy due to dipole electromagnetic emission. Next, we have the one with only one charged black hole, due to additional loss of energy in the electromagnetic emission. Finally, the system with black holes with the same charge is the last to merge, as it has to fight against additional electrostatic repulsion.

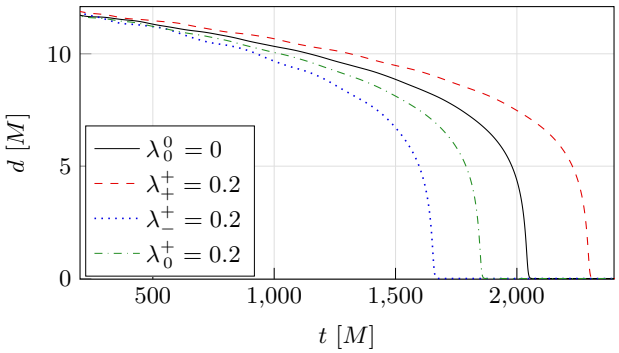


FIG. 7. Coordinate distance of the two black holes as a function of the coordinate time for three representative cases with charge-to-mass ratio of $\lambda = 0.2$, along with the case with no electromagnetic fields. Note that this is not a gauge-independent plot.

An important first finding is that for a fixed binary mass corresponding to GW150914, the SNR and the number of in-band gravitational-wave cycles depend very weakly on the charge: $\lesssim 3\,\%$. This is in spite of the different evolutions depicted in Fig. 7. This result will likely change if we consider low-mass binaries, which have a much longer inspiral that can be significantly affected by the presence of charge earlier in the inspiral.

### 1. *Properties of the emission*

In this subsection, we explore some properties of the electromagnetic and gravitational emission. We find that

TABLE II. Summary of relative errors for key quantities across all our simulations. The relative error for a quantity $\Upsilon$ is computed as $(\Upsilon^{\rm QA}-\Upsilon^{\rm NR})/\Upsilon^{\rm NR}$, where $\Upsilon^{\rm QA}$ is the quantity in the quadrupole approximation and $\Upsilon^{\rm NR}$ in the simulations. The relative error is with sign: positive error means that the Newtonian approximation *overestimates* the quantity. In all cases the quadrupole approximation overestimates the quantities. The values of the reference frequencies is reported in Table I. GW and EM indicate gravitational and electromagnetic waves respectively. When it comes to loss of angular momentum due to electromagnetic waves, the QA model only includes the dipolar channel, which is identically zero in the ++ case. Hence, we do not report this error for this quantity.

| Relative error | $f_0 \to f_1$ | | | $f_0 \to f_2$ | | |
|---|---|---|---|---|---|---|
| $[(\Upsilon^{\rm QA}-\Upsilon^{\rm NR})/\Upsilon^{\rm NR}]$ | ++ | +− | +0 | ++ | +− | +0 |
| Time | 22 % – 26 % | 15 % – 24 % | 20 % – 24 % | 26 % – 29 % | 18 % – 27 % | 24 % – 27 % |
| Phase | 20 % – 32 % | 18 % – 30 % | 17 % – 30 % | 20 % – 32 % | 18 % – 30 % | 17 % – 30 % |
| GW cycles | 24 % – 26 % | 15 % – 25 % | 21 % – 25 % | 24 % – 26 % | 15 % – 25 % | 21 % – 25 % |
| GW energy | 47 % – 48 % | 34 % – 47 % | 42 % – 47 % | 56 % – 59 % | 42 % – 56 % | 52 % – 56 % |
| EM energy | 42 % – 44 % | 59 % – 76 % | 70 % – 76 % | 47 % – 51 % | 76 % – 99 % | 91 % – 98 % |
| GW angular momentum | 45 % – 48 % | 35 % – 45 % | 41 % – 46 % | 54 % – 57 % | 42 % – 54 % | 51 % – 55 % |
| EM angular momentum | – | 57 % – 70 % | 53 % – 58 % | – | 71 % – 87 % | 65 % – 69 % |
| GW150914-like SNR | 13 % – 23 % | 23 % – 26 % | 21 % – 23 % | 20 % – 28 % | 65 % – 69 % | 19 % – 21 % |

in our simulations several quantities of interest scale with $\lambda^2$. This scaling is expected to be exact in the limit where the charge has a negligible contribution to the dynamics, and it will likely stop to be valid for larger values of $\lambda$, where the self-gravity of the electromagnetic fields becomes more important. Even if we do not expect these relations to hold, they are still useful because the charge-to-mass ratios explored here are up to 0.3, which is a considerable amount of charge (corresponding to 30 % of the maximum value allowed for a general-relativistic black hole).

First, we notice that the energy and angular momentum lost in gravitational-wave emission depend only weakly on the value of $\lambda$ for the cases considered in our set. This is shown in the top panel of Fig. 8, where we plot the total energy lost by gravitational waves for the various simulations we performed.

Next, it is interesting to study which modes dominate the emission. We focus on the $\lambda = 0.3$ simulations, and begin with the electromagnetic sector. Based on Newtonian arguments, we expect that in black hole binaries with opposite charge, most of the emission will be dipolar. By contrast, for simulations with like charge we expect no dipole, overall reduced emission, mostly in the quadrupole. Finally, the case with only one charged black hole (which has a non-zero dipole) should lie in between. The bottom panel of Fig. 8 shows the total energy carried away by electromagnetic waves starting at the reference frequency $f_0$ until peak gravitational wave amplitude, and demonstrates that the aforementioned intuition is correct. Moreover, the figure shows that the energy emitted scales with the charge-to-mass ratio squared. When computing the mode-by-mode contributions to the electromagnetic emission, we find that for the $\lambda_-^+$ case, $\ell = 1$ dominates over all other modes and constitutes 98 % of the energy lost. For $\lambda_+^+$ the $\ell = 2$ mode is the main channel through which energy is carried away, and 98 % is lost in this way. In the $\lambda_0^+$ case both dipole and quadrupole are important, the first contributing 78 %, and the second 20 %. Higher order modes constitute less than 2 % contribution. In all of our simulations the $\ell = 2$ mode accounts for 98 % of the energy lost by gravitational waves. If we considered angular momentum instead of energy, we arrive at similar conclusions.

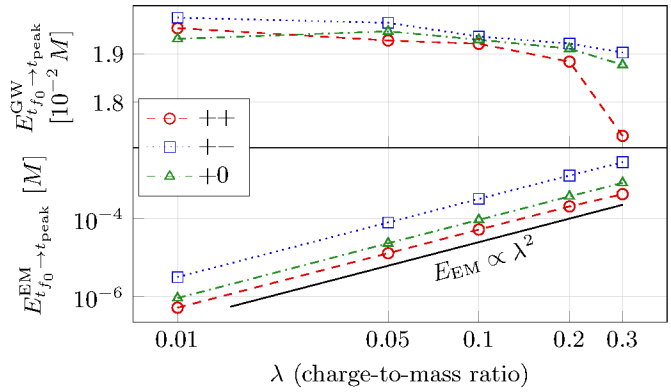


FIG. 8. Top: total energy radiated away in gravitational waves (between frequencies $f_0$ and $f_{\rm peak}$) as a function of $\lambda$ for the different cases we simulated. Bottom: total energy radiated away in electromagnetic waves $E_{\rm EM}$ as a function of $\lambda$. We find that the energy scales as the charge squared for for the cases considered in this work. The simulation that radiates the most is the one with opposite charges because its electric dipole is the largest. In the same-charge case, the emission is dominated by the electric quadrupole and it is still significant. The angular momentum lost by waves behaves similarly.

The bottom panel in Fig. 8 demonstrates that the emitted electromagnetic energy scales as $\lambda^2$. That is not the only quantity that does so. We find that several quantities scale the same way, including $E_{\rm EM}$, $J_{\rm EM}$, $E_{\rm EM}/E_{\rm GW}$, and $J_{\rm EM}/J_{\rm GW}$. We observe an example of this in Fig. 9 which shows $E_{\rm EM}/E_{\rm GW}$, and $J_{\rm EM}/J_{\rm GW}$ vs $\lambda$. As remarked at the beginning of this subsection, while we find the scaling with $\lambda^2$ for several quantities, it is possible that some of this relationships will fail for larger

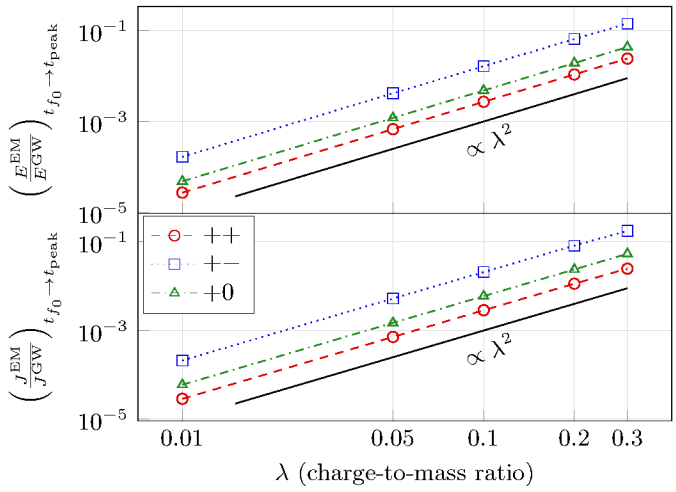


FIG. 9. Ratio between electromagnetic and gravitational energy and angular momentum lost via emission of radiation from $t_{f_0}$ to merger. The configuration with the strongest electromagnetic emission is the one with opposite charges, as the dipole is the most effective as emitting.

values of the charge.

In [44] it was estimated that for equal-mass mergers and black holes endowed with opposite charges,

$$E^{+-}_{\rm EM}/E^{+-}_{\rm GW} \approx 2\lambda^2\,. \tag{42}$$

Using our results, which strictly speaking do not apply to the equal mass case but should be close enough, we find

$$E^{+-}_{\rm EM}/E^{+-}_{\rm GW} \approx 1.6\lambda^2\,. \tag{43}$$

Thus, in spite of the simple derivation in [44], the expression provided finds the correct order of magnitude in the numerical coefficient.

If we consider charge in its traditional meaning of electric charge, we can talk about electromagnetic luminosity emitted. For the simulations with $\lambda = 0.3$, the peak electromagnetic luminosity varies from $2.7\times10^{-5}$ to $8.6\times10^{-5}$, corresponding to $\approx 10^{57}$ erg s$^{-1}$ (regardless of the value of $M$). For $M = 65\,M_\odot$, the maximum electromagnetic energy emitted is $\approx 10^{53}$ erg , which is much smaller than the energy emitted through gravitational waves. This possibly explains the near perfect scaling with $\lambda^2$ of several quantities we reported. How this electromagnetic energy is converted to potentially observable photons has to be modeled and it is highly dependent on the environment. In standard astrophysical conditions, the diluted plasma would not allow these waves to propagate [78].

### 2. *Charge detectability*

In this subsection, we use our simulation results to estimate black hole charge detectability by future gravitational wave detectors. To do this, we follow [2] and compute the mismatch between two signals $h_1$ and $h_2$. This quantity determines the minimum SNR needed to distinguish $h_1$ and $h_2$, which we denote as $\mathrm{SNR}(h_1,h_2)$, and is given by [63, 152–155]

$$\mathrm{SNR}(h_1,h_2) = \frac{1}{\sqrt{2}}\frac{1}{\sqrt{\mathrm{mismatch}(h_1,h_2)}}\,. \tag{44}$$

Note that the SNR threshold value of Eq. (44) corresponds to a 68 % confidence level for distinguishability. We compute the mismatch as [2, 155, 156]

$$\mathrm{mismatch}(h_1,h_2) = 1 - \max \mathcal{O}(h_1,h_2)\,, \tag{45}$$

with the maximum evaluated with respect to time-shifts, polarization angles, and mass shifts. We maximize over mass shifts to include the possible degeneracy between mass and charge (see [2] for a detailed discussion). This operation is allowed because our simulations scale with the total mass $M$. In Eq. (45), $\mathcal{O}(h_1,h_2)$ is the overlap between $h_1$ and $h_2$

$$\mathcal{O}(h_1,h_2) = \frac{(h_1,h_2)}{\sqrt{(h_1,h_1)(h_2,h_2)}}\,, \tag{46}$$

with $(h_1,h_2)$ being the noise-weighted inner product between the two signals in the frequency domain $\tilde{h}_1(f)$ and $\tilde{h}_2(f)$, which is given by [157]

$$(h_1,h_2) = 4\mathrm{Re}\int_{f_{\rm min}}^{f_{\rm max}} \frac{\tilde{h}_1(f)\tilde{h}_2^\star(f)}{S_n(f)}\,\mathrm{d}f\,, \tag{47}$$

where $S_n(f)$ is the power spectral density of the detector noise, and the asterisk indicates complex conjugation. In the subsequent analysis we consider the following detectors at design sensitivity: Advanced LIGO, A+ [158], Voyager [159], Einstein Telescope [160], and Cosmic Explorer [161] and we set $f_{\rm min} = 25\,$Hz and $f_{\rm max} = 1024\,$Hz.[9]. Note that here we are not including the effects of spins, mass-ratios, and eccentricity, parameters that introduce degeneracies that make the detection of charge more difficult. Nonetheless, the key result of this subsection will hold at a more qualitative level even when the additional parameters are included: for a GW510914-like event, future instruments are expected to detect signals with a SNR significantly larger than the one needed to detect charge at the level of $\lambda \approx 0.1$. For precision studies, more accurate simulations that include also the other parameters are needed.

[9] When available, we use the sensitivity curves implemented in LALSimulation [162] via PyCBC [163]. The functions used are part of the `pycbc.psd` module and are: `aLIGODesignSensitivityP1200087`, `aLIGOAPlusDesignSensitivityT1800042`, `EinsteinTelescopeP1600143`, and `CosmicExplorerP1600143`. For Voyager we obtained the sensitivity curve from LIGO Document T1500293-v11.

Before we discuss the results, we highlight possible pitfalls in numerically evaluating Eq. (47). There are multiple steps to go from what the simulations output to Eq. (47). In particular, Fourier transforms have to be computed and the time series have to be windowed and zero-padded to avoid aliasing and spectral leakage. Since the simulations we are considering produce similar waveforms (up to time, phase, and mass shifts), small differences in how the two waves are pre-processed can contribute significantly to the value of the mismatch. First, it is important to trim the end of the two waveforms where the strain is practically zero and ensure that they have the same duration after the peak. If this is not done, and the signals have different durations after merger, applying a window has a different effect and introduces a systematic uncertainty. Second, in some cases the fixed frequency integration may leave small residual drifts at the very end of the waveform. These depend on the simulation, so one must check that all the waves are well-behaved. In case they are not, one can adjust this by cropping the signal or by changing the parameters of the window function or of the integration method. Improperly considering one of these effects may lead to systematic errors.

We now discuss the results of our study by focusing on the $\lambda_-^+$ case, which is relevant to constraining the dipole emission. In Fig. 10, we report the value of the SNR needed to distinguish uncharged binary waveforms from binary black holes with charge-to-mass ratio $\lambda_-^+ = 0.1$ (circles), 0.2 (stars), or 0.3 (diamonds) for a GW150914-like event. For smaller values of $\lambda_-^+$, the mismatch computed from our simulations is limited by their numerical error, so higher resolution evolutions would be needed.

First, we note that there is not much variation of the SNR for distinguishability across the different detectors, regardless of the significant variation in sensitivity. The reason for this result is that for the computation of the mismatch the overall noise curve does not matter: it is how the noise is distributed in different frequencies that matters the most. The difference in sensitivity is reflected in how easy or not it is to achieve such SNRs. Second, the values needed to detect $\lambda_-^+ \geq 0.1$ are already achievable today (GW150914 had a network-SNR of approximately 25 [69], but its noise curve was not the one at deign sensitivity). Given their improved sensitivity, future detectors will immediately be able to detect this amount of charge. To estimate what limits on charge future detectors will place, one not only needs better simulations, but one needs to include the effects of spin and eccentricity.

Next, we discuss what charge-to-mass ratio LISA would be able to detect for million solar mass binaries. As already mentioned, we are free to rescale the mass of our binaries to place them in the LISA band, which we assume ranges from 0.1 mHz to 1 Hz. Despite the scale freedom, there is one obstacle to doing a complete analysis using our simulation data as Fig. 11 demonstrates. In the plot, we show the LISA sensitivity curve [164] and we schematically show with dashed lines the gravitational wave spectrum from our simulations when the mass is rescaled using two different values. In the case of a $10^7 M_\odot$ binary, our simulation signal is entirely in the LISA band. On the other hand, at least part of the inspiral is missing for $\sim 10^{4-6} M_\odot$ binaries.[10] Despite this obstacle, we know that for the case with opposite charge, the mismatch will increase if we included the inspiral, due to the presence of dipole emission. Hence, if we use our data to find what is the minimum SNR needed to distinguish waveforms of charged binaries from those generated by uncharged binaries, we will find an upper bound on that (if we included the entire in-band inspiral waveform the minimum SNR for distinguishability would only decrease).

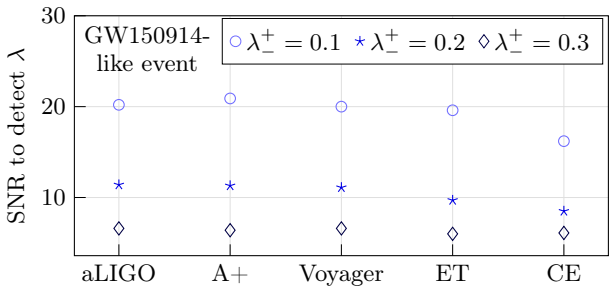


FIG. 10. Signal-to-noise ratio required to distinguish waveforms from mergers of charged black holes from ones without charge for different detectors assuming their design sensitivity. The expected SNR for a GW150914-like event future detectors is significantly larger than the one needed to constrain $\lambda_-^+ < 0.1$. See Footnote 9 for details on the detector sensitivity curves used.

[10] One could extended our simulation data with some approximate waveforms, like the one from the Newtonian model, and recompute the quantities with the entire signal. However, this goes beyond the scope of the current work.

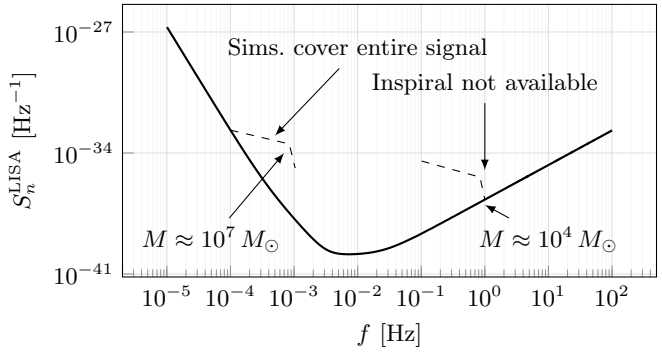


FIG. 11. Schematic representation of how we can use our simulations for LISA sources. We are free to vary the mass, but in many cases our simulations do not cover the entirety of the signal, and part of the inspiral is missing. Since the inspiral is the most constraining part of the signal, when we compute the minimum SNR for distinguishability of charged binary waveforms from uncharged binary ones, we are providing an upper bound.

Figure 12 shows the upper bound on the minimum SNR needed to distinguish waveforms generated by charged binaries from those generated by uncharged binaries for different charge configurations as a function of the detector-frame mass $M_{\rm detector}$. LISA is expected to detect binaries with SNR much higher than the one in Fig. 12, so it will be able to detect or place constraints on small values of $\lambda_-^+$ for multiple systems. These results are not surprising. In [44, 71] it argued that LISA will constrain the dipole moment at the level of the $10^{-4}$, considering only the inspiral.

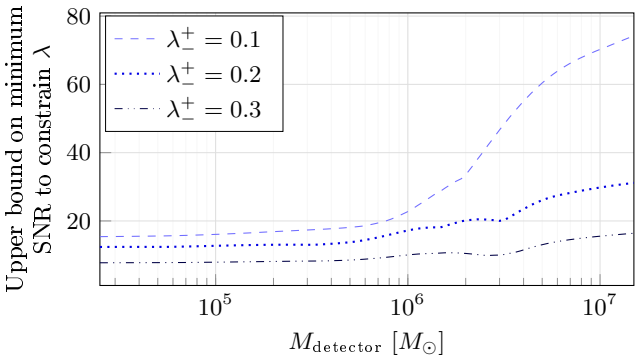


FIG. 12. Upper limit on the minimum SNR needed to distinguish waveform from charged binaries with different $\lambda_-^+$ from uncharted systems. This is an upper limit because most of the masses do not include the entirety of the inspiral. Given that the inspiral is most constraining, including it would decrease the SNR needed.

We can understand the shape in Fig. 12 by considering that the inspiral has the most important contribution to the mismatch, so, it is the lower frequencies that matter the most. Recall that Fig. 11 shows schematically the power spectrum of the gravitational waves. Roughly speaking, there is more power in the lower frequencies than the higher ones because more time is spent there. Increasing the binary mass from the minimum value considered here amounts to sliding the spectrum in Fig. 11 from the right to the left. When we are considering masses for which the signal lies to the right-hand-side of the plot, we find that there is more noise in the higher frequencies of the signal than the lower ones. This is the optimal condition to separate an uncharged waveform from a charged ones, because it is the lower frequencies that contain the most information. Hence, the signal to noise for the detection is the lowest. Now, when we consider masses for which the signal lies on the left-hand-side of Fig. 11, initially not much changes in the signal-to-noise ratio. This is because the frequencies with the most information are the ones with the lowest noise. The scenario changes when we approach the minimum of the sensitivity curve, at that point, the way noise is distributed across frequency changes, and we see in Fig. 12 an increase in the signal-to-noise ratio, which reflects the fact that we are removing sensitivity in the lower frequencies to put it in the higher ones (that have less information). The trend continues when we increase further the mass scale and we climb up the sensitivity curve on the left side. Here, we are giving more weight to high frequencies, which cannot distinguish the two waves well, so we need more signal-to-noise ratio for distinguishability of two signals.

A natural question that arises next is the following: how far can LISA detect the minimum SNR required to distinguish charge? Computing the SNR with Eq. (40b), we can find what is the maximum distance at which the SNR is larger than the threshold. This distance is plotted in Fig. 13. For some mass ranges, LISA will essentially distinguish a charged binary with $\lambda_-^+$ up to 0.1 everywhere it can detect black hole binaries. It is important to note that that plot provides only a lower limit on this maximum distance, especially for lower masses, where we do not include the long inspiral part of the waveform.

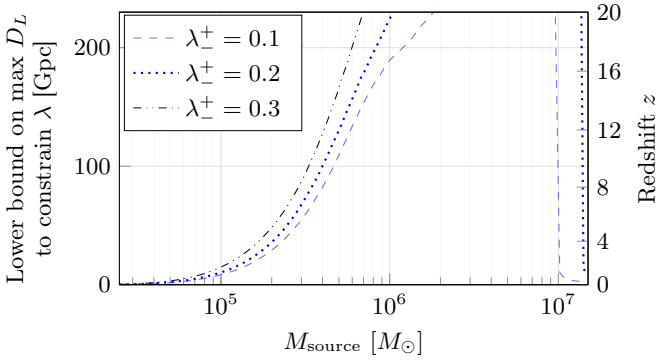


FIG. 13. Lower limit on the maximum luminosity distance $D_L$ in gigaparsec (or max redshift $z$) at which LISA can detect a charged binary with $\lambda$ of 0.1 as function of the source-frame mass $M_{\rm source}$.

We can ask the same question for the case $\lambda_+^+ = 0.3$ at the mass-scale for which we have the entire signal in

LISA band ($\approx 10^7\,M_\odot$). We find that LISA will be able to detect charge up to redshift of about 1, which would translate to a constraint on the $\alpha$ parameter of Moffat's Scalar-Vector-Tensor gravity [19] of $\alpha \lesssim 0.1$ (see also, [2]).

### C. Properties of the remnant black hole and ringdown

Here we study the properties of the remnant black hole forming following the merger of charged binaries. We discuss the accuracy of the method presented in Sec. IV A to estimate the remnant black hole spin (Sec. V C 1), and we explore the quasi-normal-modes from the ringdown phase (Sec. V C 2).

#### 1. *Remnant black hole properties*

In this subsection, we discuss the physical properties of the charged binary black hole merger remnants in our numerical-relativity simulations as computed via `QuasiLocalMeasuresEM`. Then, we compare the remnant black hole spin found in the simulations with the expectations of the BKL approximation described in Sec. IV A.

Before presenting our results, let us consider what one might expect qualitatively. Following the discussion in Sec. II B, we know that, in Newtonian physics, the orbital angular momentum scales as $\sqrt{G}$. Next, consider conservation of angular momentum, and assume (as in the BKL method) that the spin of the final black hole is determined by the angular momentum at the innermost-stable circular orbit of the remnant black hole. We would expect the final spin $\chi^{\rm final}$ with respect to the uncharged case $\chi^{\rm final}_{00}$ to increase as $\sqrt{1-\lambda_1\lambda_2}$ for the case with opposite charge (where the ISCO of the remnant black hole is the same as in the uncharged case[11]), and to decrease faster than $\sqrt{1-\lambda_1\lambda_2}$ for the other two cases, where the ISCO is reduced compared to the uncharged case, resulting in additional emission of angular momentum.

In Fig. 14 we show how these properties change with respect to their values in the uncharged case. First, we find that the final mass of the remnant is almost independent of the charge configuration, with sub-percent variations. In particular, the $\lambda^+_-$ remnant looks almost identical to the one from the uncharged simulation: spin, charge, and mass are the same to within 1 %. Moreover, in that case, the angular momentum is essentially independent of $\lambda$, against the expectations from the Newtonian argument. In general, we find that the final properties of the black hole depend weakly on the charge configuration, with the largest variation being about 4 % in the spin of the $\lambda^+_+ = 0.3$ case. Interestingly, the cases with like charge follow the Newtonian scaling $\sqrt{1-\lambda_1\lambda_2}$ as shown in Fig. 14 with the black solid lines.

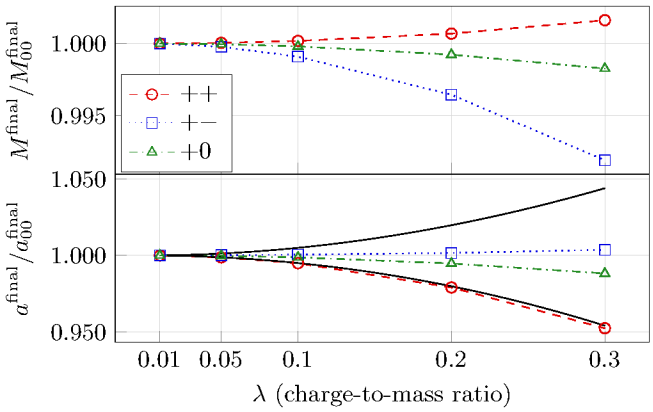


FIG. 14. Mass (top panel) and spin (bottom panel) of the remnant black hole computed with the isolated horizon formalism [115, 165, 166] as implemented in `QuasiLocalMeasuresEM` [1], compared to the one in a merger with no charge ($M^{\rm final}_{00} \approx 0.96\,M$, $a^{\rm final}_{00} \approx 0.66\,M$). The solid black lines in the bottom panel indicate the Newtonian scaling $\sqrt{1 \pm \lambda_1\lambda_2}$.

In Sec. IV A, we described a simple way to estimate the spin of the remnant using conservation arguments. We now compare the method with our simulations. The top panel of Fig. 15 shows that the method estimates the value of the final dimensionless spin with an error of 3 % in the uncharged case. This method does not include energy loss. Including it would not improve accuracy, as the dimensionless spin would be overestimated as opposed to underestimated. In the bottom panel of Fig. 15 we normalize the final spin to the value of the uncharged case with simulations normalized with the values obtained from the simulations, and the BKL values are normalized with the value obtained applying the method in absence of charge. This removes the normalization as a possible parameter and allows us to test if the method captures the correct trend (and only gets the normalization wrong). In practice, this corresponds to testing whether removing trends arising from the normalization makes the black lines in the bottom panel of Fig. 15 overlap with the colored ones. We observe that the method indeed works well for the cases with like charge or with only one charged black hole, but overestimates the final spin in the other cases. The approach does not capture the fact that the spin of the final black hole in the $\lambda^+_-$ numerical relativity simulations is essentially independent of charge. However, the method is still accurate to within a few per cent.

[11] Although the ISCO of the remnant black hole in the charged case with opposite charges is practically unaffected by charge (for the range of $\lambda$ in this work), since the total charge is approximately zero, the effective innermost stable orbit of the binary (the orbital separation at plunge) must be affected to some extend, especially for larger values of $\lambda$ even when the component black holes have exactly opposite charges.

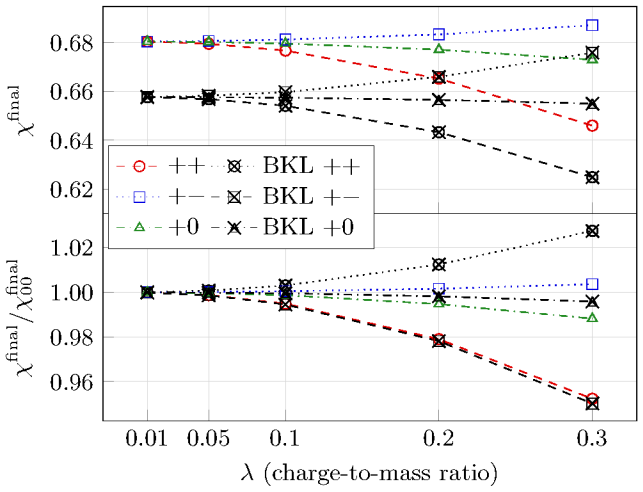


FIG. 15. Dimensionless spin of the remnant black hole in the numerical relativity simulations (colored lines) and estimated with the method of Sec. IV (black lines with crossed markers). In the top panel, we compare the actual numerical values, in the bottom panel we rescale the values by the value measured in the simulation without charge or the estimated value in absence of charge (simulation data is normalized with the value obtained from the uncharged simulation, and BKL estimates are normalized with the value obtained assuming no charge).

### 2. *Quasi-normal-modes*

Here we discuss the ring-down phase and address how challenging it is to tell if a binary black hole is charged from the ringdown phase alone.

Since the frequency and decay time of the quasi-normal-modes depend only on mass, spin, and charge, we can use the values reported in Fig. 14 to compute $\omega_{220}$ and $\tau_{220}$ with Eqs. (39) and the `qnm` code [145]. The top panel of Fig. 16 shows the relative difference of the computed value $(\omega_{220} - \omega^{00}_{220})/\omega^{00}_{220}$, where $\omega^{00}_{220}$ is the ring-down frequency computed with `qnm` using the mass and spin of the remnant black hole from the simulation without charge, while $\omega_{220}$ is the ring-down frequency using Eqs. (39). The maximum difference we find is 0.9 % in the $\lambda^+_- = 0.3$ case. Therefore, to be able to distinguish the ringdown from a merger of charged black holes from one with no charge, the parameters have to be estimated better than the percent level. For a given value of $\lambda$, even higher accuracy is needed to be able to distinguish the three charged scenarios.

It is interesting to understand why the simulation with opposite charge, in which the remnant has the least amount of total charge for a fixed $\lambda$, is the one with largest difference with respect to the uncharged case: In Fig. 15, we see that for the case with opposite charges $\chi^{\rm final}/\chi^{\rm final}_{00} \approx 1$ regardless of the value of $\lambda$. Combining this information with the fact that the remnant black hole has $Q/M \ll 1$, we deduce that the only difference between the uncharged case and the case with $\lambda^+_- = 0.3$ must be in the mass of the final black hole. The difference in mass alone is responsible for the observed difference in the ringdown frequencies.

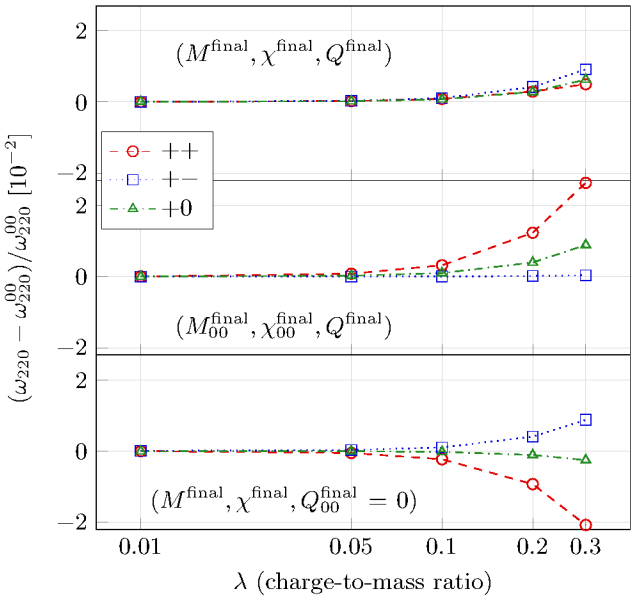


FIG. 16. Relative difference between the analytical 220 quasi-normal-mode frequency for the merger remnants in our evolutions and the simulation with uncharged black holes. In the middle panel, we remove the effects of mass and spin and fix the values to the ones they have in the uncharged case. In the bottom panel, we remove the contribution of the charge described by Eqs. (39): the frequency becomes more different. The same happens with the decay time, but the variation with respect to the uncharged case is even smaller.

It is also interesting to understand why the case with same charge is not the easiest to distinguish, despite that the remnant black hole mass in this case has $\lambda \approx 0.3$, and is the one with the most different spin (Fig. 15) compared to the uncharged case. Interestingly, in the $\lambda^+_+$ case, charge, angular momentum and mass conspire so that the remnant black hole appears to have a quasi-normal mode frequency that matches that from an uncharged binary. To analyze this case, it is convenient to separate the effects of charge, and mass and spin. The fundamental properties of the quasi-normal-modes, $\omega_{220}$ and $\tau_{220}$, depend on the triplet $(M^{\rm final}, \chi^{\rm final}, Q^{\rm final})$. We can hold some of these parameters fixed to the case with no charges to understand what is the dominant contribution to the deviation of $\omega_{220}$ and $\tau_{220}$ from their corresponding values in the absence of charge. The results are reported in the middle and bottom panels of Fig. 16, where we report $\omega_{220}$. The same results hold for $\tau_{220}$.

In the middle panel we vary only the charge, and fix the mass and spin to the value they obtain in the simulation with no charge $M^{\rm final}_{00}$ and $\chi^{\rm final}_{00}$. Here we find that binaries with opposite charge have remnant black holes that behave almost exactly like the uncharged one (there is no difference in the quasi-normal-modes). This tells us that for this specific configuration the deviation in $\omega_{220}$ is not

because of charge, but that the mass and spin are the parameters that primarily control the quasi-normal-modes properties. This is not unexpected: oppositely charged binaries are those with the smallest remnant black hole charge, so it is natural that this parameter will contribute the least if mass and angular momentum are the same. On the other hand, the case with like charges is the most different from the uncharged ones, with relative increase in $\omega_{220}$ of 2.6 %.

The bottom panel of Fig. 16 shows what happens when we completely ignore the contribution of charge to the quasi-normal modes. First, we find the confirmation that here is where the simulations $\lambda^{+}_{-}$ acquire the differences of up to $\approx 1\,\%$ shown in the top panel of Fig. 16. Second, in the like charges case, we also find that charge introduces differences in the mass and angular momentum of the remnant black hole that drive the change in the quasi-normal mode in the opposite direction compared to the ones shown in the middle panel. Therefore, when we consider the complete triplet of mass, spin, and charge ("summing" middle and bottom panels), we find that their effects almost cancel each other, so that the corresponding quasi-normal-modes are close to the uncharged binary case.

Hence, we conclude that for the $\lambda$ explored here, to distinguish the quasi-normal modes of the final black hole from the ones of an uncharged black hole, one needs exquisite accuracy. The task becomes even harder when one includes the other parameters which we kept fixed in our simulation (mass-ratio, spin, and eccentricity), which will introduce additional degeneracies. The accuracy needed is also of the same order as that of the fitting functions in Eq. (39), and for the highest values of $\lambda$ adopted here, it is also of the same order as the errors due to the truncation of the expansion in $\lambda$, which may affect the result. In our simulations, the ringdown signals are essentially indistinguishable from one another, and we cannot identify the quasi-normal-mode parameters at the accuracy needed to tell them apart. To sum up, values of charge up to $\lambda \sim 0.3$ could be challenging to detect using the ring-down phase alone.

## VI. CONCLUSIONS AND FUTURE DIRECTIONS

In this paper, we continued our program of exploring the non-linear dynamics of black holes in Einstein-Maxwell theory. In Sec. II, we described our theoretical and numerical approach, emphasizing new features and formalism that have not been treated before, including: how to prepare quasi-circular initial data for charged black hole binaries (Sec. II B), how to perform long-term and stable evolutions of quasi-circular inspirals of charged black holes (Sec. II C), the electromagnetic contribution to horizon properties of black holes (Sec. II D), and the computation of the angular momentum carried away by electromagnetic waves with the Newman-Penrose formalism (Sec. II E).

We compared the results of our non-linear simulations with approximate approaches for the inspiral (Sec. V A) and the ringdown (Sec. V C). For the systems considered, our work shows that Newtonian models based on the quadrupole approximation find the correct order of magnitude in a set of gauge-invariant quantities, but have errors $\mathcal{O}(20\%)$ or larger, and hence they cannot be used in precision studies of mergers of charged black holes or accurate parameter estimation. Similarly, estimates of the spin of the remnant black hole based on conservation of angular momentum and energy arguments are accurate up to few percent. Hence, a key result of this work is extending what was found in [20]: these arguments can be used to build intuition and make order-of-magnitude estimates in the case of quasi-circular mergers, too.

Furthermore, we discussed properties of the emission (Sec. V B) and estimated the detectability of charge by future gravitational wave observatories (Sec. V B 2), focusing in particular on LISA. Finally, we studied the quasi-normal-modes (Sec. V C 2), finding that it may be challenging to extract charge information from the ringdown alone.

There are multiple possible extensions of this work. On the non-linear side, including spin and increasing the charge-to-mass ratio would allow the exploration of a region of the parameter space never considered before. On the side of approximate calculations, the next step in complexity after Newtonian physics is developing 1PN models. Such waveforms are currently available [167, 168]. These models are important in the effort of generating gravitational-wave templates.

## ACKNOWLEDGMENTS

We used `kuibit` [169] for part of our analysis. We thank M. Zilhão for help with `ProcaEvolve`. We are grateful to the developers and maintainers of the open-source codes that we used. This work was in part supported by NSF Grant PHY-1912619 to the University of Arizona. G. B. is supported by a Texas Advanced Computing Center (TACC) Frontera Fellowship. Frontera is supported by NSF grant No. OAC-1818253. We acknowledge the hospitality of the Kavli Institute for Theoretical Physics (KITP), where part of the work was conducted. KITP is partially supported by the NSF grant No. PHY-1748958. Computational resources were provided by the Extreme Science and Engineering Discovery Environment (XSEDE) under grant number TG-PHY190020. XSEDE is supported by the NSF grant No. ACI-1548562. Simulations were performed on `Comet`, and `Stampede2`, which is funded by the NSF through award ACI-1540931.

### Appendix A: Courant stability of Kreiss-Oliger Dissipation

Kreiss-Oliger dissipation is described by Eq. (7), which we rewrite here for convenience

$$\partial_t U = \cdots + (-1)^{(p+3)/2} \frac{\epsilon}{2^{p+1}} \Delta x^p \partial_x^{p+1} U \,. \tag{A1}$$

This technique has a free a parameter $\epsilon$ that controls the strength of the dissipation. This cannot be chosen arbitrarily, as we show in this Appendix.

A finite-difference discretization transforms Eq. (7) to

$$\partial_t U = \cdots + (-1)^{(p+3)/2} \frac{\epsilon}{2^{p+1}} \Delta x^p \frac{D^{p+1} U}{\Delta x^{p+1}} \,, \tag{A2}$$

where $D^{p+1}U$ is determined by the finite-difference stencil. For an explicit time integration scheme, this operator alone leads to a Courant stability condition of the form

$$\frac{\Delta t}{\Delta x} \frac{\epsilon}{2^{p+1}} \leq \Lambda \,, \tag{A3}$$

where $\Lambda$ is typically a fixed number that is determined by the details of numerical integration method.[12] Given that in our case we add dissipation to hyperbolic partial differential equations, condition (A3) can be recast to read

$$\epsilon \leq \frac{\Lambda}{\mu} \,, \tag{A4}$$

where $\mu$ is the Courant factor $\Delta t/\Delta x$. For the Einstein-Maxwell equations in standard finite-difference implementations, this quantity is typically chosen such that $\mu \leq 0.5$ for numerical stability. Since we are working with an adaptive-mesh-refinement computational grid with sub-cycling in time, there are multiple values of $\Delta t$ and of $\Delta x$, so condition (A3) can be met in some parts of the grid but not in others. Failure to satisfy the condition can result in numerical instabilities that spoil the simulation. It should be noted that the Courant condition (A4) is necessary but not sufficient for stability. This means that the scheme can be unstable even when Eq. (A4) is satisfied. For example, an ill-posed initial boundary value problem or other numerical instabilities could cause simulations to crash.

### Appendix B: Parameters of the numerical evolution

In this Appendix, we report the parameters used for our simulations, including the test described in Sec. II C.

Our simulations are on a grid with outer boundary at $1033\,M$ and nine refinement levels with refinement boundaries located at $2^i M$, where $i$ is the number of level. Our standard coarsest-level resolution is $\approx 4\,M$ and the high-resolution runs are with 25 % smaller grid spacing ($\approx 3.2\,M$). Of the nine refinement levels, five have the same timestep, the other levels had Courant factor fixed to $\Delta t/\Delta x$ of 0.4. This choice reduces the maximum timestep on the grid and prevents some numerical instability that would otherwise arise. We set $\kappa$ (defined in Appendix A in [23]) to $9.9\,M^{-1}$ and verified that changing this parameter does not produce significant differences. We set the $\eta$ parameter in the evolution of the shift vector (as defined in Eq. (13) in [88]) to $1.5\,M^{-1}$. These parameters lead to instability unless $\kappa \lesssim 1.5/\Delta t_{\rm max}$ (same for $\eta$), so we adjusted the time-stepping in our evolutions to ensure that this condition is met. We use fifth order prolongation in space and second in time. We tested selected cases with seventh order spatial prolongation and found no significant differences. All our derivatives are obtained with sixth-order finite difference.

The test described in Sec. II C was performed with the high-resolution grid and otherwise the same parameters described above. The tests showed that the instabilities arise unless we choose the continuous prescription for the dissipation. In the unstable cases, we found that simulations with higher resolution become unstable earlier compared to the ones at lower resolution.

In Fig. 17, we report how resolution and extraction radii affect the resulting waveform. The differences between the various signals are small, indicating the error due to the finite resolution and finite extraction radius does not affect the results presented in this paper.

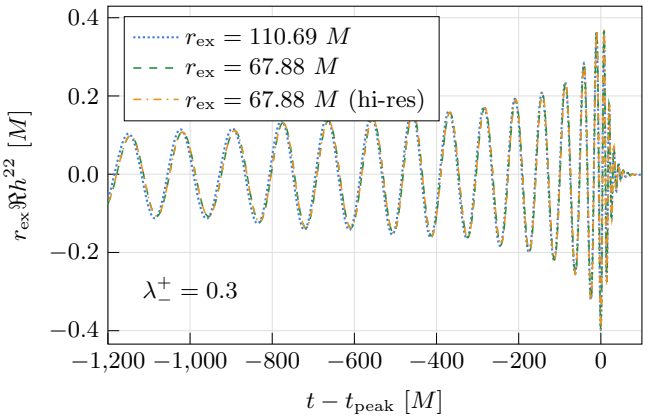


FIG. 17. Real part of the $l = 2$, $m = 2$ strain extracted from different radii or different resolutions from the simulation with $\lambda_-^+ = 0.3$. The three waveforms agree well, indicating that the error due to the finite resolution or the finite extraction radius is small.

[12] The case with $p = 1$ using standard centered second-order accurate finite differences is a textbook example of stability analysis for a standard diffusion equation with constant coefficients. In this case, and for a three-dimensional Cartesian grid with equal grid spacing in the all spatial directions, $\Lambda = 1/6$.

### Appendix C: Alternative formulations

In our efforts to improve and stabilize our simulations, we tested two additional formulations for the evolution of the electromagnetic fields. We found that improvements arising from either of these formulations is subdominant compared to the role of the dissipation (see, Sec. II C).

First, we followed [170] and implemented a generalized Lorenz condition. If $A_a$ is the electromagnetic four-potential, the Lorenz gauge is $\nabla_a A^a = 0$, while its generalized version is $\nabla_a A^a = \xi n_a A^a$, with $\xi$ damping parameter. In [170], it was found that with a suitable choice of $\xi$, this condition reduces spurious gauge modes that arise from interpolation at the refinement level boundaries. While this is important for general-relativistic magnetohydrodynamic simulations in which matter crosses refinement levels, in our evolutions we did not find significant improvements.

A second formulation we tested was motivated by the parabolized Arnowitt-Deser-Misner formalism of general relativity [171, 172]. This consists of adding an extra parabolic term to the evolution of the electric field, which is 0 when the Gauss constraint is satisfied,

$$\partial_t E^i = \cdots + \epsilon_E \gamma^{ij} \partial_j C_E \,. \tag{C1}$$

with $C_E$ is the Gauss constraint and $\epsilon_E$ strength of the parabolic term. With this modification, the evolution of the constraint looks like

$$\partial_t C_E = \cdots + \epsilon_E \gamma^{ij} \partial_i \partial_j C_E \,, \tag{C2}$$

which is parabolic diffusion operator. The indented result is to further dissipate violations of the constraint from perturbations with high wave number. In our tests, this formulation did not result in noticeable improvements over our new method for setting the Kreiss-Oliger dissipation parameter presented in Sec. II C.

### Appendix D: Newman-Penrose scalars in flat spacetime as function of electric and magnetic fields

In this Appendix, we provide expressions for the electromagnetic Newman-Penrose $\Phi_0$, $\Phi_1$, and $\Phi_2$ in terms of the electric and magnetic fields in (asymptotically) flat spacetime. We consider both coordinate and orthonormal bases. These expressions can be used to quickly compute the Newman-Penrose scalars for a given electromagnetic field. (For a similar discussion, see Appendix A in [173] noting that a different convention is used for the normalization of the tetrad.)

In flat spacetime and given the spherical coordinates $(r, \theta, \varphi)$, consider the coordinate basis $(\boldsymbol{\partial}_r, \boldsymbol{\partial}_\theta, \boldsymbol{\partial}_\phi)$, and an orthonormal basis $(\boldsymbol{e}_{\hat{r}}, \boldsymbol{e}_{\hat{\theta}}, \boldsymbol{e}_{\hat{\phi}})$ so that for a vector $\boldsymbol{v}$ we have that

$$\boldsymbol{v} = v^{\hat{r}} \boldsymbol{e}_{\hat{r}} + v^{\hat{\theta}} \boldsymbol{e}_{\hat{\theta}} + v^{\hat{\varphi}} \boldsymbol{e}_{\hat{\varphi}} \,, \tag{D1a}$$

$$\boldsymbol{v} = v^{r} \boldsymbol{\partial}_{r} + v^{\theta} \boldsymbol{\partial}_{\theta} + v^{\hat{\varphi}} \boldsymbol{\partial}_{\varphi} \,, \tag{D1b}$$

with

$$v^{\hat{r}} = v^r \,, \qquad v_{\hat{r}} = v_r \,, \tag{D2a}$$

$$v^{\hat{\theta}} = r v^\theta \,, \qquad v_{\hat{\theta}} = \frac{1}{r} v_\theta \,, \tag{D2b}$$

$$v^{\hat{\varphi}} = r \sin\theta v^\varphi \,, \qquad v_{\hat{\varphi}} = \frac{1}{r \sin\theta} v_\varphi \,. \tag{D2c}$$

The electromagnetic field strength can be written in terms of the orthonormal tetrad components of the electric and magnetic fields as follows

$$F_{ab} = \begin{pmatrix} 0 & -E_{\hat{r}} & -rE_{\hat{\theta}} & -r\sin\theta E_{\hat{\varphi}} \\ E_{\hat{r}} & 0 & rB_{\hat{\varphi}} & -r\sin\theta B_{\hat{\theta}} \\ rE_{\hat{\theta}} & -rB_{\hat{\varphi}} & 0 & r^2\sin\theta B_{\hat{r}} \\ r\sin\theta E_{\hat{\varphi}} & r\sin\theta B_{\hat{\theta}} & -r^2\sin\theta B_{\hat{r}} & 0 \end{pmatrix} . \tag{D3}$$

The Newman-Penrose scalars are, as computed by Eqs. (8) and using Eq. (D3)

$$\Phi_0 = \frac{1}{2}\left(-E_{\hat{\theta}} + B_{\hat{\varphi}} - i(E_{\hat{\varphi}} + B_{\hat{\theta}})\right) \,, \tag{D4a}$$

$$\Phi_1 = \frac{1}{2}\left(E_{\hat{r}} + iB_{\hat{r}}\right) \,, \tag{D4b}$$

$$\Phi_2 = \frac{1}{2}\left(E_{\hat{\theta}} + B_{\hat{\varphi}} - i(E_{\hat{\varphi}} - B_{\hat{\theta}})\right) \,. \tag{D4c}$$

Alternatively, expressing Eqs. (D4) in terms of the vector components in the coordinate basis:

$$\Phi_0 = \frac{1}{2}\left[-\frac{E_\theta}{r} + \frac{B_\varphi}{r\sin\theta} - i\left(\frac{E_\varphi}{r\sin\theta} + \frac{B_\theta}{r}\right)\right] \,, \tag{D5a}$$

$$\Phi_1 = \frac{1}{2}\left(E_r + iB_r\right) \,, \tag{D5b}$$

$$\Phi_2 = \frac{1}{2}\left[\frac{E_\theta}{r} + \frac{B_\varphi}{r\sin\theta} - i\left(\frac{E_\varphi}{r\sin\theta} - \frac{B_\theta}{r}\right)\right] \,. \tag{D5c}$$

For completeness, we also report the null tetrad of Eq. (13) is (in the coordinate basis)

$$k^a = \frac{1}{\sqrt{2}}(1, -1, 0, 0) \,, \tag{D6a}$$

$$l^a = \frac{1}{\sqrt{2}}(1, 1, 0, 0) \,, \tag{D6b}$$

$$m^a = \frac{1}{\sqrt{2}}\left(0, 0, \frac{1}{r}, \frac{i}{r\sin\theta}\right) \,, \tag{D6c}$$

$$m^{*a} = \frac{1}{\sqrt{2}}\left(0, 0, \frac{1}{r}, -\frac{i}{r\sin\theta}\right) \,. \tag{D6d}$$

### Appendix E: Michel's solution

Michel's rotating magnetic monopole solution [126] is a simple model for pulsar and black hole magnetospheres (for a rigorous description, see [127], noting that Heaviside-Lorentz units are used, and many formulas differ by a factor of $4\pi$ with what is reported here). Our interest in Michel's monopole is motivated by the fact

that it is a simple solution with stationary flow of energy and angular momentum in flat spacetime that can be used to test Eq. (17) and its numerical implementation.

In an orthonormal basis, the non-zero components of electric and magnetic fields of Michel's monopole are [127]

$$E_{\hat{\theta}} = B_{\hat{\varphi}} = -\frac{q}{r}\omega \sin\theta \,, \tag{E1a}$$

$$B_{\hat{r}} = \frac{q}{r^2} \,. \tag{E1b}$$

A four-vector potential that produces such configuration is given by

$$A_{\hat{\mu}} = \left( q\omega\cos\theta, 0, -\frac{q}{r}\omega\sin\theta, q\tan\frac{\theta}{2} \right) \,. \tag{E2}$$

Notice that $A_{\hat{\varphi}} \to +\infty$ when $\theta \to \pi$, but the resulting magnetic field is well-behaved, as shown in Eq. (E1b).

We can compute the Newman-Penrose scalars $\Phi_1$ and $\Phi_2$ with Eqs. (D4):

$$\Phi_1 = -\frac{q}{r}\omega\sin\theta \,, \tag{E3a}$$

$$\Phi_2 = \frac{i}{2}\frac{q}{r^2} \,. \tag{E3b}$$

As expected, $\Phi_1$ and $\Phi_2$ follow the peeling behavior of Eqs. (9). Next, we can use Eq. (15) to compute the total power that crosses a sphere or radius $r$

$$\frac{\mathrm{d}E_{\rm EM}}{\mathrm{d}t} = \frac{2}{3}q^2\omega^2 \,. \tag{E4}$$

We can also compute the flux of angular momentum along the $z$ direction radiated with Eq. (17)

$$\frac{\mathrm{d}L^z_{\rm EM}}{\mathrm{d}t} = \frac{2}{3}q^2\omega \,. \tag{E5}$$

Hence, we find the relation

$$\frac{\mathrm{d}E_{\rm EM}}{\mathrm{d}t} = \omega\frac{\mathrm{d}L^z_{\rm EM}}{\mathrm{d}t} \,. \tag{E6}$$

This is a well-known relation for pulsar and black hole magnetospheres.


[1] G. Bozzola and V. Paschalidis, Phys. Rev. D **99**, 104044 (2019), arXiv:1903.01036 [gr-qc].
[2] G. Bozzola and V. Paschalidis, Phys. Rev. Lett. **126**, 041103 (2021), arXiv:2006.15764 [gr-qc].
[3] Event Horizon Telescope Collaboration, Astrophys. J. Lett. **875**, L1 (2019), arXiv:1906.11238 [astro-ph.GA].
[4] B. P. Abbott, R. Abbott, T. D. Abbott, S. Abraham, F. Acernese, K. Ackley, C. Adams, R. X. Adhikari, V. B. Adya, C. Affeldt, and et al., Physical Review X **9**, 031040 (2019), arXiv:1811.12907 [astro-ph.HE].
[5] B. P. Abbott, R. Abbott, T. D. Abbott, M. R. Abernathy, F. Acernese, K. Ackley, C. Adams, T. Adams, P. Addesso, R. X. Adhikari, and et al., Physical Review Letters **116**, 221101 (2016), arXiv:1602.03841 [gr-qc].
[6] K. Yagi and L. C. Stein, Classical and Quantum Gravity **33**, 054001 (2016), arXiv:1602.02413 [gr-qc].
[7] B. P. Abbott, R. Abbott, T. D. Abbott, S. Abraham, F. Acernese, K. Ackley, C. Adams, R. X. Adhikari, V. B. Adya, C. Affeldt, and et al., Phys. Rev. D **100**, 104036 (2019), arXiv:1903.04467 [gr-qc].
[8] B. P. Abbott, R. Abbott, T. D. Abbott, F. Acernese, K. Ackley, C. Adams, T. Adams, P. Addesso, R. X. Adhikari, V. B. Adya, and et al. (LIGO Scientific Collaboration and Virgo Collaboration), Phys. Rev. Lett. **123**, 011102 (2019).
[9] N. Yunes, K. Yagi, and F. Pretorius, Phys. Rev. D **94**, 084002 (2016), arXiv:1603.08955 [gr-qc].
[10] J. Cayuso, N. Ortiz, and L. Lehner, Phys. Rev. D **96**, 084043 (2017), arXiv:1706.07421 [gr-qc].
[11] E. W. Hirschmann, L. Lehner, S. L. Liebling, and C. Palenzuela, Phys. Rev. D **97**, 064032 (2018), arXiv:1706.09875 [gr-qc].
[12] J. L. Ripley and F. Pretorius, Class. Quant. Grav. **37**, 155003 (2020), arXiv:2005.05417 [gr-qc].
[13] W. E. East and J. L. Ripley, Phys. Rev. D **103**, 044040 (2021), arXiv:2011.03547 [gr-qc].
[14] M. Okounkova, L. C. Stein, M. A. Scheel, and D. A. Hemberger, Phys. Rev. D **96**, 044020 (2017), arXiv:1705.07924 [gr-qc].
[15] M. Okounkova, L. C. Stein, J. Moxon, M. A. Scheel, and S. A. Teukolsky, Phys. Rev. D **101**, 104016 (2020), arXiv:1911.02588 [gr-qc].
[16] H. Witek, L. Gualtieri, P. Pani, and T. P. Sotiriou, Phys. Rev. D **99**, 064035 (2019), arXiv:1810.05177 [gr-qc].
[17] M. Okounkova, Phys. Rev. D **102**, 084046 (2020), arXiv:2001.03571 [gr-qc].
[18] H. Witek, L. Gualtieri, and P. Pani, Phys. Rev. D **101**, 124055 (2020), arXiv:2004.00009 [gr-qc].
[19] J. W. Moffat, J. Cosm. Astropart. Phys. **2006**, 004 (2006), arXiv:gr-qc/0506021 [gr-qc].
[20] M. Zilhão, V. Cardoso, C. Herdeiro, L. Lehner, and U. Sperhake, Phys. Rev. D **85**, 124062 (2012), arXiv:1205.1063 [gr-qc].
[21] M. Zilhão, V. Cardoso, C. Herdeiro, L. Lehner, and U. Sperhake, Phys. Rev. D **89**, 044008 (2014), arXiv:1311.6483 [gr-qc].
[22] M. Zilhão, V. Cardoso, C. Herdeiro, L. Lehner, and U. Sperhake, Phys. Rev. D **90**, 124088 (2014), arXiv:1410.0694 [gr-qc].
[23] M. Zilhão, H. Witek, and V. Cardoso, Classical Quant. Grav. **32**, 234003 (2015), arXiv:1505.00797 [gr-qc].
[24] S. L. Liebling and C. Palenzuela, Phys. Rev. D **94**, 064046 (2016), arXiv:1607.02140 [gr-qc].
[25] R. M. Wald, Phys. Rev. D **10**, 1680 (1974).
[26] G. W. Gibbons, Communications in Mathematical Physics **44**, 245 (1975).

[27] D. M. Eardley and W. H. Press, Ann. Rev. Astron. Astrophys. **13**, 381 (1975).
[28] Y. Gong, Z. Cao, H. Gao, and B. Zhang, Mon. Not. R. Astron. Soc. **488**, 2722 (2019), arXiv:1907.05239 [gr-qc].
[29] Z. Pan and H. Yang, Phys. Rev. D **100**, 043025 (2019), arXiv:1905.04775 [astro-ph.HE].
[30] J. L. Feng, M. Kaplinghat, H. Tu, and H.-B. Yu, J. Cosm. Astropart. Phys. **2009**, 004 (2009), arXiv:0905.3039 [hep-ph].
[31] L. Ackerman, M. R. Buckley, S. M. Carroll, and M. Kamionkowski, Phys. Rev. D **79**, 023519 (2009), arXiv:0810.5126 [hep-ph].
[32] R. Foot and S. Vagnozzi, Phys. Rev. D **91**, 023512 (2015), arXiv:1409.7174 [hep-ph].
[33] R. Foot and S. Vagnozzi, Physics Letters B **748**, 61 (2015), arXiv:1412.0762 [hep-ph].
[34] R. Foot and S. Vagnozzi, J. Cosm. Astropart. Phys. **2016**, 013 (2016), arXiv:1602.02467 [astro-ph.CO].
[35] P. Agrawal, F.-Y. Cyr-Racine, L. Randall, and J. Scholtz, JCAP **05**, 022, arXiv:1610.04611 [hep-ph].
[36] Ø. Christiansen, J. B. Jiménez, and D. F. Mota, Classical Quant. Grav. **38**, arXiv:2003.11452 (2021), arXiv:2003.11452 [gr-qc].
[37] S. Davidson, B. Campbell, and D. Bailey, Phys. Rev. D **43**, 2314 (1991).
[38] M. L. Perl and E. R. Lee, American Journal of Physics **65**, 698 (1997).
[39] S. Davidson, S. Hannestad, and G. Raffelt, Journal of High Energy Physics **5**, 003 (2000), hep-ph/0001179.
[40] S. L. Dubovsky, D. S. Gorbunov, and G. I. Rubtsov, Soviet Journal of Experimental and Theoretical Physics Letters **79**, 1 (2004), arXiv:hep-ph/0311189 [astro-ph].
[41] S. Chatrchyan, V. Khachatryan, A. M. Sirunyan, A. Tumasyan, W. Adam, E. Aguilo, Bergauer, and et al., Phys. Rev. D **87**, 092008 (2013), arXiv:1210.2311 [hep-ex].
[42] A. D. Dolgov, S. L. Dubovsky, G. I. Rubtsov, and I. I. Tkachev, Phys. Rev. D **88**, 117701 (2013), arXiv:1310.2376 [hep-ph].
[43] H. Vogel and J. Redondo, J. Cosm. Astropart. Phys. **2014**, 029 (2014), arXiv:1311.2600 [hep-ph].
[44] V. Cardoso, C. F. B. Macedo, P. Pani, and V. Ferrari, J. Cosm. Astropart. Phys. **5**, 054 (2016), arXiv:1604.07845 [hep-ph].
[45] P. Gautham A. and S. Sethi, J. Cosm. Astropart. Phys. **2020**, 039 (2020), arXiv:1910.04779 [astro-ph.CO].
[46] R. Plestid, V. Takhistov, Y.-D. Tsai, T. Bringmann, A. Kusenko, and M. Pospelov, arXiv e-prints , arXiv:2002.11732 (2020), arXiv:2002.11732 [hep-ph].
[47] L. Liu, Z.-K. Guo, R.-G. Cai, and S. P. Kim, Phys. Rev. D **102**, 043508 (2020), arXiv:2001.02984 [astro-ph.CO].
[48] L. Liu, Ø. Christiansen, Z.-K. Guo, R.-G. Cai, and S. P. Kim, Phys. Rev. D **102**, 103520 (2020), arXiv:2008.02326 [gr-qc].
[49] L. Liu, Ø. Christiansen, Z.-K. Guo, R.-G. Cai, and S. P. Kim, arXiv e-prints , arXiv:2011.13586 (2020), arXiv:2011.13586 [gr-qc].
[50] Y. Bai, J. Berger, M. Korwar, and N. Orlofsky, Journal of High Energy Physics **2020**, 210 (2020), arXiv:2007.03703 [hep-ph].
[51] D. Ghosh, A. Thalapillil, and F. Ullah, Phys. Rev. D **103**, 023006 (2021), arXiv:2009.03363 [hep-ph].
[52] B. P. Abbott *et al.* (LIGO Scientific Collaboration and Virgo Collaboration), Phys. Rev. Lett. **116**, 061102 (2016), 1602.03837.
[53] M. Hannam, S. Husa, J. A. González, U. Sperhake, and B. Brügmann, Phys. Rev. D **77**, 044020 (2008), arXiv:0706.1305 [gr-qc].
[54] I. MacDonald, S. Nissanke, and H. P. Pfeiffer, Classical and Quantum Gravity **28**, 134002 (2011), arXiv:1102.5128 [gr-qc].
[55] P. Ajith, M. Boyle, D. A. Brown, B. Brügmann, L. T. Buchman, L. Cadonati, M. Campanelli, T. Chu, Z. B. Etienne, S. Fairhurst, M. Hannam, J. Healy, I. Hinder, S. Husa, and others., Classical Quant. Grav. **29**, 124001 (2012), arXiv:1201.5319 [gr-qc].
[56] J. Aasi, B. P. Abbott, R. Abbott, T. Abbott, M. R. Abernathy, T. Accadia, F. Acernese, K. Ackley, C. Adams, T. Adams, and et al., Classical and Quantum Gravity **31**, 115004 (2014), arXiv:1401.0939 [gr-qc].
[57] A. K. Mehta, C. K. Mishra, V. Varma, and P. Ajith, Phys. Rev. D **96**, 124010 (2017), arXiv:1708.03501 [gr-qc].
[58] V. Varma, S. E. Field, M. A. Scheel, J. Blackman, L. E. Kidder, and H. P. Pfeiffer, Phys. Rev. D **99**, 064045 (2019), arXiv:1812.07865 [gr-qc].
[59] B. S. Sathyaprakash and S. V. Dhurandhar, Phys. Rev. D **44**, 3819 (1991).
[60] S. V. Dhurandhar and B. S. Sathyaprakash, Phys. Rev. D **49**, 1707 (1994).
[61] R. Balasubramanian, B. S. Sathyaprakash, and S. V. Dhurandhar, Phys. Rev. D **53**, 3033 (1996), arXiv:gr-qc/9508011 [gr-qc].
[62] É. É. Flanagan and S. A. Hughes, Phys. Rev. D **57**, 4535 (1998), gr-qc/9701039.
[63] É. É. Flanagan and S. A. Hughes, Phys. Rev. D **57**, 4566 (1998), gr-qc/9710129.
[64] B. Aylott, J. G. Baker, W. D. Boggs, M. Boyle, P. R. Brady, D. A. Brown, B. Brügmann, L. T. Buchman, A. Buonanno, L. Cadonati, J. Camp, M. Campanelli, J. Centrella, S. Chatterji, N. Christensen, T. Chu, P. Diener, N. Dorband, Z. B. Etienne, *et al.*, Classical Quant. Grav. **26**, 165008 (2009), arXiv:0901.4399 [gr-qc].
[65] I. Hinder *et al.*, Class. Quant. Grav. **31**, 025012 (2014), arXiv:1307.5307 [gr-qc].
[66] V. E. Hubeny, Phys. Rev. D **59**, 064013 (1999), arXiv:gr-qc/9808043 [gr-qc].
[67] R. M. Wald, International Journal of Modern Physics D **27**, 1843003 (2018).
[68] H. Kreiss and J. Oliger, *Methods for the Approximate Solution of Time Dependent Problems*, Global Atmospheric Research Programme (GARP): GARP Publication Series, Vol. 10 (GARP Publication, 1973).
[69] B. P. Abbott, R. Abbott, T. D. Abbott, M. R. Abernathy, F. Acernese, K. Ackley, C. Adams, T. Adams, P. Addesso, R. X. Adhikari, and et al., Physical Review Letters **116**, 241102 (2016), arXiv:1602.03840 [gr-qc].
[70] H.-T. Wang, P.-C. Li, J.-L. Jiang, Y.-M. Hu, and Y.-Z. Fan, arXiv e-prints , arXiv:2004.12421 (2020), arXiv:2004.12421 [gr-qc].
[71] V. Cardoso, C. F. B. Macedo, P. Pani, and V. Ferrari, J. Cosm. Astropart. Phys. **2020**, E01 (2020).
[72] P. Amaro-Seoane, H. Audley, S. Babak, J. Baker, E. Barausse, P. Bender, E. Berti, P. Binetruy, M. Born, D. Bortoluzzi, J. Camp, C. Caprini, V. Cardoso, M. Colpi, J. Conklin, N. Cornish, C. Cutler, K. Danzmann, R. Dolesi, L. Ferraioli, V. Ferroni, E. Fitzsimons,

J. Gair, L. Gesa Bote, D. Giardini, F. Gibert, C. Grimani, H. Halloin, G. Heinzel, T. Hertog, M. Hewitson, K. Holley-Bockelmann, D. Hollington, M. Hueller, H. Inchauspe, P. Jetzer, N. Karnesis, C. Killow, A. Klein, B. Klipstein, N. Korsakova, S. L. Larson, J. Livas, I. Lloro, N. Man, D. Mance, J. Martino, I. Mateos, K. McKenzie, S. T. McWilliams, C. Miller, G. Mueller, G. Nardini, G. Nelemans, M. Nofrarias, A. Petiteau, P. Pivato, E. Plagnol, E. Porter, J. Reiche, D. Robertson, N. Robertson, E. Rossi, G. Russano, B. Schutz, A. Sesana, D. Shoemaker, J. Slutsky, C. F. Sopuerta, T. Sumner, N. Tamanini, I. Thorpe, M. Troebs, M. Vallisneri, A. Vecchio, D. Vetrugno, S. Vitale, M. Volonteri, G. Wanner, H. Ward, P. Wass, W. Weber, J. Ziemer, and P. Zweifel, arXiv e-prints , arXiv:1702.00786 (2017), arXiv:1702.00786 [astro-ph.IM].

[73] E. Berti, V. Cardoso, and C. M. Will, Phys. Rev. D **73**, 064030 (2006), gr-qc/0512160.

[74] P. Jaiakson, A. Chatrabhuti, O. Evnin, and L. Lehner, Phys. Rev. D **96**, 044031 (2017), arXiv:1706.06519 [gr-qc].

[75] R. Arnowitt, S. Deser, and C. W. Misner, General Relativity and Gravitation **40**, 1997 (2008).

[76] C. W. Misner, K. S. Thorne, and J. A. Wheeler, *General relativity* (W.H. Freeman and Co., San Francisco, CA, 1973).

[77] R. M. Wald, *General relativity* (Chicago Univ. Press, Chicago, IL, 1984).

[78] V. Cardoso, W.-D. Guo, C. F. B. Macedo, and P. Pani, Mon. Not. R. Astron. Soc. **503**, 563 (2021), arXiv:2009.07287 [gr-qc].

[79] M. Alcubierre, *Introduction to 3+1 Numerical Relativity* (Oxford University Press, UK, 2008).

[80] T. W. Baumgarte and S. L. Shapiro, *Numerical Relativity: Solving Einstein's Equations on the Computer* (Cambridge University Press, 2010).

[81] M. Shibata, *Numerical Relativity* (World Scientific Publishing Co, 2016).

[82] F. Löffler, J. Faber, E. Bentivegna, T. Bode, P. Diener, R. Haas, I. Hinder, B. C. Mundim, C. D. Ott, E. Schnetter, G. Allen, M. Campanelli, and P. Laguna, Class. Quantum Grav. **29**, 115001 (2012), arXiv:1111.3344 [gr-qc].

[83] Collaborative Effort, Einstein Toolkit for Relativistic Astrophysics, Astrophysics Source Code Library (2011), ascl:1102.014.

[84] EinsteinToolkit, Einstein Toolkit: Open software for relativistic astrophysics (2019).

[85] J. M. Bowen and J. York, James W., Phys. Rev. D **21**, 2047 (1980).

[86] J. M. Bowen, Annals of Physics **165**, 17 (1985).

[87] M. Ansorg, B. Brügmann, and W. Tichy, Phys. Rev. D **70**, 064011 (2004), gr-qc/0404056.

[88] U. Sperhake, Phys. Rev. D **76**, 104015 (2007), gr-qc/0606079.

[89] M. Shibata and T. Nakamura, Phys. Rev. D **52**, 5428 (1995).

[90] T. W. Baumgarte and S. L. Shapiro, Phys. Rev. D **59**, 024007 (1998).

[91] M. Alcubierre, B. Brügmann, T. Dramlitsch, J. A. Font, P. Papadopoulos, E. Seidel, N. Stergioulas, and R. Takahashi, Phys. Rev. D **62**, 044034 (2000), arXiv:gr-qc/0003071.

[92] M. Alcubierre, B. Brügmann, P. Diener, M. Koppitz, D. Pollney, E. Seidel, and R. Takahashi, Phys. Rev. D **67**, 084023 (2003), arXiv:gr-qc/0206072.

[93] H. Witek, M. Zilhao, G. Ficarra, and M. Elley, Canuda: a public numerical relativity library to probe fundamental physics (2020).

[94] H. Witek and M. Zilhão, Canuda code (2015), `https://bitbucket.org/canuda/`.

[95] J. Thornburg, Phys. Rev. D **54**, 4899 (1996), arXiv:gr-qc/9508014.

[96] J. Thornburg, Class. Quantum Grav. **21**, 743 (2004), arXiv:gr-qc/0306056.

[97] O. Dreyer, B. Krishnan, D. Shoemaker, and E. Schnetter, Phys. Rev. D **67**, 024018 (2003), arXiv:gr-qc/0206008.

[98] C. Reisswig and D. Pollney, Classical Quant. Grav. **28**, 195015 (2011), arXiv:1006.1632 [gr-qc].

[99] E. Schnetter, S. H. Hawley, and I. Hawke, Class. Quantum Grav. **21**, 1465 (2004), arXiv:gr-qc/0310042.

[100] H. P. Pfeiffer, D. A. Brown, L. E. Kidder, L. Lindblom, G. Lovelace, and M. A. Scheel, Class. Quantum Grav. **24**, S59 (2007), arXiv:gr-qc/0702106.

[101] K. Levenberg, Quarterly of Applied Mathematics **2**, 164 (1944).

[102] D. W. Marquardt, Journal of the Society for Industrial and Applied Mathematics **11**, 431 (1963).

[103] M. Pürrer, S. Husa, and M. Hannam, Phys. Rev. D **85**, 124051 (2012), arXiv:1203.4258 [gr-qc].

[104] A. Ramos-Buades, S. Husa, and G. Pratten, Phys. Rev. D **99**, 023003 (2019), arXiv:1810.00036 [gr-qc].

[105] F. Pretorius, Phys. Rev. Lett. **95**, 121101 (2005), arXiv:gr-qc/0507014.

[106] J. G. Baker, J. Centrella, D.-I. Choi, M. Koppitz, and J. van Meter, Phys. Rev. Lett. **96**, 111102 (2006), arXiv:gr-qc/0511103.

[107] M. Campanelli, C. O. Lousto, P. Marronetti, and Y. Zlochower, Phys. Rev. Lett. **96**, 111101 (2006), arXiv:gr-qc/0511048.

[108] Y. Zlochower, J. G. Baker, M. Campanelli, and C. O. Lousto, Phys. Rev. D **72**, 024021 (2005), arXiv:gr-qc/0505055 [gr-qc].

[109] G. Calabrese, I. Hinder, and S. Husa, Journal of Computational Physics **218**, 607 (2006), arXiv:gr-qc/0503056 [gr-qc].

[110] S. Husa, J. A. González, M. Hannam, B. Brügmann, and U. Sperhake, Classical and Quantum Gravity **25**, 105006 (2008), arXiv:0706.0740 [gr-qc].

[111] M. C. Babiuc, S. Husa, D. Alic, I. Hinder, C. Lechner, E. Schnetter, B. Szilágyi, Y. Zlochower, N. Dorband, D. Pollney, and J. Winicour, Classical and Quantum Gravity **25**, 125012 (2008), arXiv:0709.3559 [gr-qc].

[112] Z. B. Etienne, J. G. Baker, V. Paschalidis, B. J. Kelly, and S. L. Shapiro, Phys. Rev. D **90**, 064032 (2014), arXiv:1404.6523 [astro-ph.HE].

[113] B. Krishnan, *Isolated Horizons in Numerical Relativity*, Ph.D. thesis, The Pennsylvania State University (2002).

[114] O. Dreyer, B. Krishnan, D. Shoemaker, and E. Schnetter, Phys. Rev. D **67**, 024018 (2003), gr-qc/0206008.

[115] A. Ashtekar, C. Beetle, and J. Lewandowski, Phys. Rev. D **64**, 044016 (2001), gr-qc/0103026.

[116] A. Ashtekar and R. O. Hansen, Journal of Mathematical Physics **19**, 1542 (1978).

[117] E. Newman and R. Penrose, Journal of Mathematical Physics **3**, 566 (1962).

[118] M. Ruiz, M. Alcubierre, D. Núñez, and R. Takahashi,

General Relativity and Gravitation **40**, 1705 (2008), arXiv:0707.4654 [gr-qc].
[119] N. T. Bishop and L. Rezzolla, Living Reviews in Relativity **19**, 2 (2016), arXiv:1606.02532 [gr-qc].
[120] H. Witek, V. Cardoso, C. Herdeiro, A. Nerozzi, U. Sperhake, and M. Zilhão, Phys. Rev. D **82**, 104037 (2010), arXiv:1004.4633 [hep-th].
[121] S. A. Teukolsky, Astrophys. J. **185**, 635 (1973).
[122] E. T. Newman and R. Penrose, Proceedings of the Royal Society of London Series A **305**, 175 (1968).
[123] A. Ashtekar and B. Bonga, General Relativity and Gravitation **49**, 122 (2017), arXiv:1707.09914 [gr-qc].
[124] B. Bonga, E. Poisson, and H. Yang, American Journal of Physics **86**, 839 (2018), arXiv:1805.01372 [physics.class-ph].
[125] B. Bonga and E. Poisson, Phys. Rev. D **99**, 064024 (2019), arXiv:1808.01288 [gr-qc].
[126] F. C. Michel, Astrophys. J. **180**, 207 (1973).
[127] S. E. Gralla and T. Jacobson, Mon. Not. R. Astron. Soc. **445**, 2500 (2014), arXiv:1401.6159 [astro-ph.HE].
[128] L. Petzold, SIAM Journal on Scientific and Statistical Computing **4** (1983).
[129] A. Hindmarsh and L. L. Laboratory, *ODEPACK, a Systematized Collection of ODE Solvers* (Lawrence Livermore National Laboratory, 1982).
[130] P. Virtfanen, R. Gommers, T. E. Oliphant, M. Haberland, T. Reddy, D. Cournapeau, E. Burovski, P. Peterson, W. Weckesser, J. Bright, S. J. van der Walt, M. Brett, J. Wilson, K. Jarrod Millman, N. Mayorov, A. R. J. Nelson, E. Jones, R. Kern, E. Larson, C. Carey, İ. Polat, Y. Feng, E. W. Moore, J. Vand erPlas, D. Laxalde, J. Perktold, R. Cimrman, I. Henriksen, E. A. Quintero, C. R. Harris, A. M. Archibald, A. H. Ribeiro, F. Pedregosa, P. van Mulbregt, and S. . . Contributors, Nature Methods **17**, 261 (2020).
[131] M. Maggiore, *Gravitational Waves. Vol. 1: Theory and Experiments*, Oxford Master Series in Physics (Oxford University Press, 2007).
[132] H. Yang, K. Yagi, J. Blackman, L. Lehner, V. Paschalidis, F. Pretorius, and N. Yunes, Phys. Rev. Lett. **118**, 161101 (2017), arXiv:1701.05808 [gr-qc].
[133] E. Berti, K. Yagi, H. Yang, and N. Yunes, General Relativity and Gravitation **50**, 49 (2018), arXiv:1801.03587 [gr-qc].
[134] E. Berti and K. D. Kokkotas, Phys. Rev. D **71**, 124008 (2005), arXiv:gr-qc/0502065 [gr-qc].
[135] V. Cardoso, A. S. Miranda, E. Berti, H. Witek, and V. T. Zanchin, Phys. Rev. D **79**, 064016 (2009), arXiv:0812.1806 [hep-th].
[136] G. Khanna and R. H. Price, Phys. Rev. D **95**, 081501 (2017), arXiv:1609.00083 [gr-qc].
[137] A. Buonanno, L. E. Kidder, and L. Lehner, Phys. Rev. D **77**, 026004 (2008), arXiv:0709.3839 [astro-ph].
[138] M. Kesden, Phys. Rev. D **78**, 084030 (2008), arXiv:0807.3043 [astro-ph].
[139] R. P. Kerr, Phys. Rev. Lett. **11**, 237 (1963).
[140] E. T. Newman, E. Couch, K. Chinnapared, A. Exton, A. Prakash, and R. Torrence, Journal of Mathematical Physics **6**, 918 (1965).
[141] H. M. Siahaan, Phys. Rev. D **101**, 064036 (2020), arXiv:1907.02158 [gr-qc].
[142] E. Berti, V. Cardoso, and A. O. Starinets, Classical Quant. Grav. **26**, 163001 (2009), arXiv:0905.2975 [gr-qc].
[143] Ringdown data.
[144] Ringdown data.
[145] L. C. Stein, J. Open Source Softw. **4**, 1683 (2019), arXiv:1908.10377 [gr-qc].
[146] Ó. J. C. Dias, M. Godazgar, and J. E. Santos, Phys. Rev. Lett. **114**, 151101 (2015), arXiv:1501.04625 [gr-qc].
[147] E. Berti, V. Cardoso, J. A. Gonzalez, U. Sperhake, M. Hannam, S. Husa, and B. Brügmann, Phys. Rev. D **76**, 064034 (2007), arXiv:gr-qc/0703053 [gr-qc].
[148] E. Barausse, A. Buonanno, S. A. Hughes, G. Khanna, S. O'Sullivan, and Y. Pan, Phys. Rev. D **85**, 024046 (2012), arXiv:1110.3081 [gr-qc].
[149] C. J. Moore, R. H. Cole, and C. P. L. Berry, Classical and Quantum Gravity **32**, 015014 (2015), arXiv:1408.0740 [gr-qc].
[150] M. Shibata and Y.-I. Sekiguchi, Phys. Rev. D **68**, 104020 (2003), arXiv:astro-ph/0402184 [astro-ph].
[151] C. Reisswig, C. D. Ott, U. Sperhake, and E. Schnetter, Phys. Rev. D **83**, 064008 (2011), arXiv:1012.0595 [gr-qc].
[152] L. Lindblom, B. J. Owen, and D. A. Brown, Phys. Rev. D **78**, 124020 (2008), arXiv:0809.3844 [gr-qc].
[153] S. T. McWilliams, B. J. Kelly, and J. G. Baker, Phys. Rev. D **82**, 024014 (2010), arXiv:1004.0961 [gr-qc].
[154] E. Baird, S. Fairhurst, M. Hannam, and P. Murphy, Phys. Rev. D **87**, 024035 (2013), arXiv:1211.0546 [gr-qc].
[155] B. P. Abbott, R. Abbott, T. D. Abbott, M. R. Abernathy, F. Acernese, K. Ackley, C. Adams, T. Adams, P. Addesso, R. X. Adhikari, and et al., Classical and Quantum Gravity **34**, 104002 (2017), arXiv:1611.07531 [gr-qc].
[156] T. Damour, B. R. Iyer, and B. S. Sathyaprakash, Phys. Rev. D **57**, 885 (1998), gr-qc/9708034.
[157] I. W. Harry and S. Fairhurst, Phys. Rev. D **83**, 084002 (2011), arXiv:1012.4939 [gr-qc].
[158] J. Miller, L. Barsotti, S. Vitale, P. Fritschel, M. Evans, and D. Sigg, Phys. Rev. D **91**, 062005 (2015), arXiv:1410.5882 [gr-qc].
[159] L. Collaboration, Instrument science white paper, ligo document ligo-t1400316-v5.
[160] M. Punturo, M. Abernathy, F. Acernese, B. Allen, N. Andersson, K. Arun, F. Barone, B. Barr, M. Barsuglia, and e. a. Beker, Classical and Quantum Gravity **27**, 194002 (2010).
[161] D. Reitze, R. X. Adhikari, S. Ballmer, B. Barish, L. Barsotti, G. Billingsley, D. A. Brown, Y. Chen, D. Coyne, R. Eisenstein, M. Evans, P. Fritschel, E. D. Hall, A. Lazzarini, G. Lovelace, J. Read, B. S. Sathyaprakash, D. Shoemaker, J. Smith, C. Torrie, S. Vitale, R. Weiss, C. Wipf, and M. Zucker, in *Bulletin of the American Astronomical Society*, Vol. 51 (2019) p. 35, arXiv:1907.04833 [astro-ph.IM].
[162] LIGO Scientific Collaboration, LIGO Algorithm Library - LALSuite, free software (GPL) (2018).
[163] A. Nitz, I. Harry, D. Brown, C. M. Biwer, J. Willis, T. D. Canton, C. Capano, L. Pekowsky, T. Dent, A. R. Williamson, M. Cabero, S. De, G. Davies, D. Macleod, B. Machenschalk, P. Kumar, S. Reyes, T. Massinger, F. Pannarale, M. Tpai, dfinstad, S. Fairhurst, S. Khan, A. Nielsen, shasvath, S. Kumar, idorrington92, L. Singer, H. Gabbard, and B. U. V. Gadre, gwastro/pycbc: Pycbc release v1.14.2 (2019).

[164] T. Robson, N. J. Cornish, and C. Liu, Classical and Quantum Gravity **36**, 105011 (2019), arXiv:1803.01944 [astro-ph.HE].
[165] A. Ashtekar, C. Beetle, O. Dreyer, S. Fairhurst, B. Krishnan, J. Lewandowski, and J. Wiśniewski, Phys. Rev. Lett. **85**, 3564 (2000), gr-qc/0006006.
[166] A. Ashtekar and B. Krishnan, Living Reviews in Relativity **7**, 10 (2004), gr-qc/0407042.
[167] F.-L. Julié, J. Cosm. Astropart. Phys. **2018**, 033 (2018), arXiv:1809.05041 [gr-qc].
[168] M. Khalil, N. Sennett, J. Steinhoff, J. Vines, and A. Buonanno, Phys. Rev. D **98**, 104010 (2018), arXiv:1809.03109 [gr-qc].
[169] G. Bozzola, The Journal of Open Source Software **6**, 3099 (2021), arXiv:2104.06376.
[170] B. D. Farris, R. Gold, V. Paschalidis, Z. B. Etienne, and S. L. Shapiro, Physical Review Letters **109**, 221102 (2012), arXiv:1207.3354 [astro-ph.HE].
[171] V. Paschalidis, Phys. Rev. D **78**, 024002 (2008), arXiv:0704.2861 [gr-qc].
[172] V. Paschalidis, J. Hansen, and A. Khokhlov, Phys. Rev. D **78**, 064048 (2008), arXiv:0712.1258 [gr-qc].
[173] T. D. Brennan, S. E. Gralla, and T. Jacobson, Classical Quant. Grav. **30**, 195012 (2013), arXiv:1305.6890 [gr-qc].